Magnetic field Amplification in a Rotating Astrophysical Plasma Sphere: α and β Effects

Kiwan Park

Soongsil University, 369, Sangdo-ro,
Dongjak-gu, Seoul 06978 Republic of Korea
pkiwan@ssu.ac.kr, pkiwan@gmail.com

(Dated: February 6, 2025)

We investigated the generation of the α and β effects in a rotating spherical plasma system with oppositely polarized kinetic helicity in the northern and southern hemispheres and examined their contributions to the induction of magnetic fields. We found that the α effect is relatively small, and its sign depends on the polarization of kinetic helicity. In contrast, the β effect remains negative regardless of the sign of kinetic helicity. Despite its small magnitude, the α effect plays a crucial role in determining the polarity of helical magnetic structures, while a negative β indicates energy diffusion from turbulent regions into the large-scale magnetic field. We derived the α and β effects with oppositely polarized kinetic helicity using different approaches, incorporating large-scale magnetic data and turbulent kinetic data. These were used to reproduce the large-scale magnetic field and compare it with DNS results. In the kinematic regime, where the magnetic field strength is weak, our results align well; however, in regions with strong nonlinear magnetic effects, the magnetic field reproduced using turbulent kinetic data diverges. This divergence is attributed to insufficient quenching of the β effect, suggesting that including the second-moment terms of velocity in the magnetic field effect would improve the accuracy of the β coefficient. In this study, we considered the case of a rotating plasma sphere with $Pr_M = 1$ and low Reynolds numbers. However, in reality, Reynolds numbers are much higher, and Pr_M is much less than 1, which necessitates further studies on this topic. We plan to address this in future research.

I. INTRODUCTION

Rotating plasma structures, such as stars, accretion disks, and other similar systems, make unique physical properties, including buoyancy and Coriolis forces. These phenomena give rise to kinetic helicity, defined as $\langle \mathbf{U} \cdot \nabla \times \mathbf{U} \rangle$, where $\mathbf{U}$ represents the fluid velocity. Kinetic helicity, in turn, generates conserved magnetic helicity $\langle \mathbf{A} \cdot \mathbf{B} \rangle$, where $\mathbf{B} = \nabla \times \mathbf{A}$. These pseudo-scalars, along with kinetic and magnetic energy, contribute to the α and β effects, which linearize the nonlinear processes governing the evolution of magnetic fields in plasmas. Moreover, these quantities play a crucial role in evolving the magnetic field profiles. The α effect amplifies the large-scale magnetic field and determines the polarity of magnetic helicity. It also couples the toroidal magnetic flux, B_{tor}, and the poloidal magnetic flux, B_{pol}, leading to their periodic evolution. Meanwhile, the β effect is traditionally associated with magnetic field diffusion, but its influence extends beyond mere magnetic dissipation.

A representative example of the magnetic field generated in the rotating spherical plasma system is the evolution of the solar magnetic field. The Sun's 22-year magnetic cycle, known as the Hale cycle, involves the strengthening, weakening, and polarity reversal of its magnetic field, reflecting internal activity and contributing to its long-term stability. As mentioned, since the evolution of the solar magnetic field can be linearly described by the α and β effects, several models have been proposed to calculate these quantities [2–5]. Parker [1955] argued that buoyancy lifts the toroidal magnetic flux, B_{tor}, and the Coriolis force twists it by $\pi/2$, forming a rotated magnetic loop. This series of processes generates the poloidal magnetic field, B_{pol}, which connects the solar north and south poles (N, S) with a phase difference of $\pi/2$. However, verifying that small-scale turbulent motion can mechanically deform the large-scale magnetic flux, which has greater magnetic energy and a longer eddy turnover time, remains challenging. Also, the significant difference in magnitude between $B_{pol}(\sim 10^{-3}\text{T})$ and $B_{\text{tor}}(0.1 - 1\text{T})$ as well as their phase difference remains unclear.

And, the Babcock-Leighton (BL, [3]) dynamo model is characterized by the transport of magnetic flux through single or multiple meridional circulation cells, along with other transport processes such as directional turbulent pumping and isotropic diffusive transport. The BL model has been successful in simulating some aspects of the solar cycle, particularly the regeneration of poloidal magnetic fields from decaying sunspots, but it also faces limitations [5]. Whether the meridional circulation and other transport processes exist as assumed remains unclear, as they depend on internal motions presupposing an inhomogeneous distribution of density and temperature in an (almost) axisymmetric system. Furthermore, the timescales and patterns of meridional circulation inferred from helioseismology are not fully consistent with the predictions of the BL model, raising questions about the robustness of the assumed flows.

These two models essentially include the α and β effects along with rotational effects. However, the α and β effects used in the Parker model (BL model) and dynamo models lack consistency with each other, and the theoretical α and β derived from dynamo
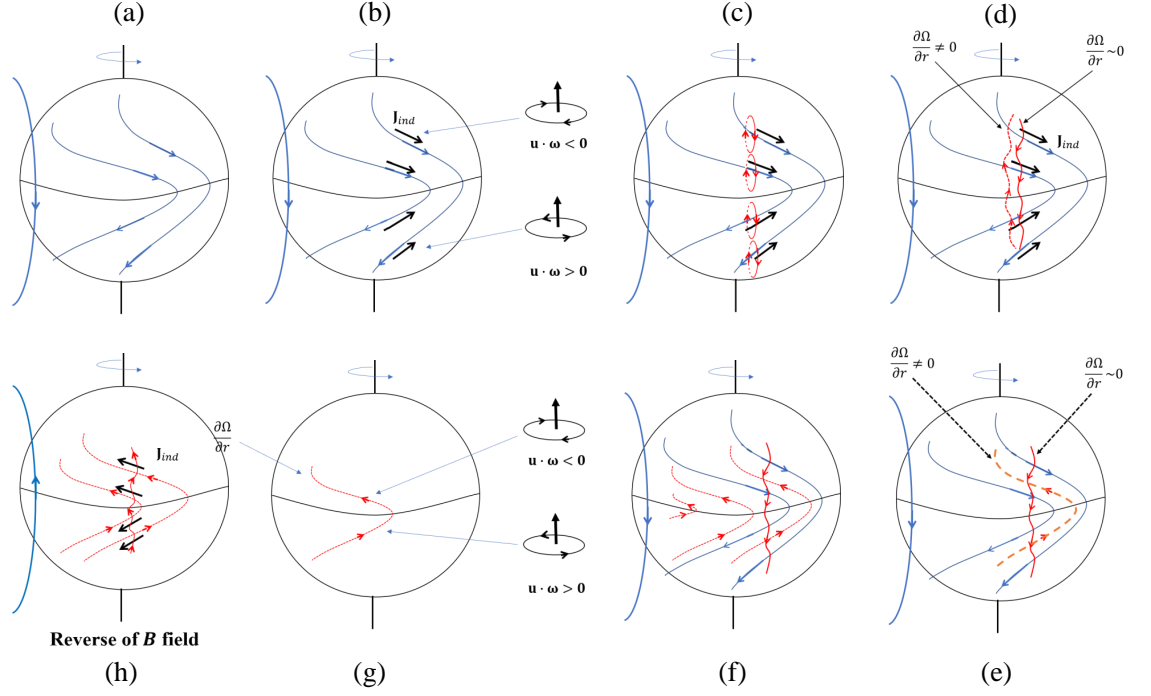
FIG. 1. This model is developed based on the physical meaning of the magnetic induction equation, unlike the Parker's model or BL model. This model is not limited to the Sun; it is applicable to rotating astrophysical plasma systems in general, where Coriolis forces and buoyancy are present. The fact that the current density flows in the same direction in both the northern and southern hemispheres results in an attractive force that helps gather the magnetic field lines toward the equator.

theory are also not yet complete. Conventionally, there have been efforts to calculate these coefficients such as mean field theory (MFT), the eddy-damped quasi-normal Markovian (EDQNM) approximation, or the direct interaction approximation (DIA) [6–8]. These theories generally suggest that α is related to residual helicity $\langle \mathbf{b} \cdot (\nabla \times \mathbf{b}) \rangle - \langle \mathbf{u} \cdot (\nabla \times \mathbf{u}) \rangle$. And, the β coefficient is thought to be related to turbulent energy $\langle u^2 \rangle$, $\langle b^2 \rangle$, but the quantities composing β in MFT, DIA, and EDQNM are not consistent. These models commonly highlight the positive β effect, i.e., magnetic diffusion. However, since these conclusions are based on the first-order incomplete approximation, it is necessary to clarify the β effect, particularly with respect to kinetic helicity.

Theoretical works have been conducted on partially negative magnetic diffusivity [9] and references therein. These studies are based on $\alpha - \alpha$ correlations in strong helical systems. Additionally, Bendre et al. [8] suggested an iterative removal of sources (IROS) method that uses the time series of the mean magnetic field and current as inputs. Experimentally, Giesecke et al. [10] found that turbulent magnetic diffusivity η_{turb} was negative. They argued that the net diffusivity $\eta_{\text{turb}} + \eta$ became positive again. Negative magnetic diffusivity was also observed in another liquid sodium experiment [11], where it was found that small-scale turbulent fluctuations ($\sim u$) contribute to the negative magnetic diffusivity in the interior region. Numerically, the Test Field Method (TFM) was introduced as a tool to extract the coefficients α and β from simulation data [12]. TFM offers a detailed breakdown of these coefficients, considering both component and position. However, using the α and β values derived from these methods, there has been no instance in which the magnetic fields obtained from observations or simulations are reproduced. Moreover, even if this is possible, it remains uncertain whether the complex theoretical methods or the artificial virtual test magnetic fields can be applied to actual observations.

To address these shortcomings, we consider the possibility of a self-consistent dynamo model based on the magnetohydrodynamic (MHD) equations, taking into account the (solar) plasma-magnetic field structure [1, 13, 14]. We aim to explain the α effect from an electromagnetic perspective and approach the β effect from the standpoint of fluid diffusion. The term α effect may resemble Parker's, but there are essential differences between them. Parker's α effect describes a series of mechanical

(a) Southern hemisphere: $\langle \mathbf{u} \cdot \omega \rangle > 0$

$$H_V = \langle \mathbf{u} \cdot \omega \rangle$$

(b) $\langle \bar{\mathbf{j}}_0 \cdot \overline{\mathbf{B}}_0 \rangle < 0$ and $\langle \mathbf{j}_1 \cdot \mathbf{b}_{ind} \rangle > 0$
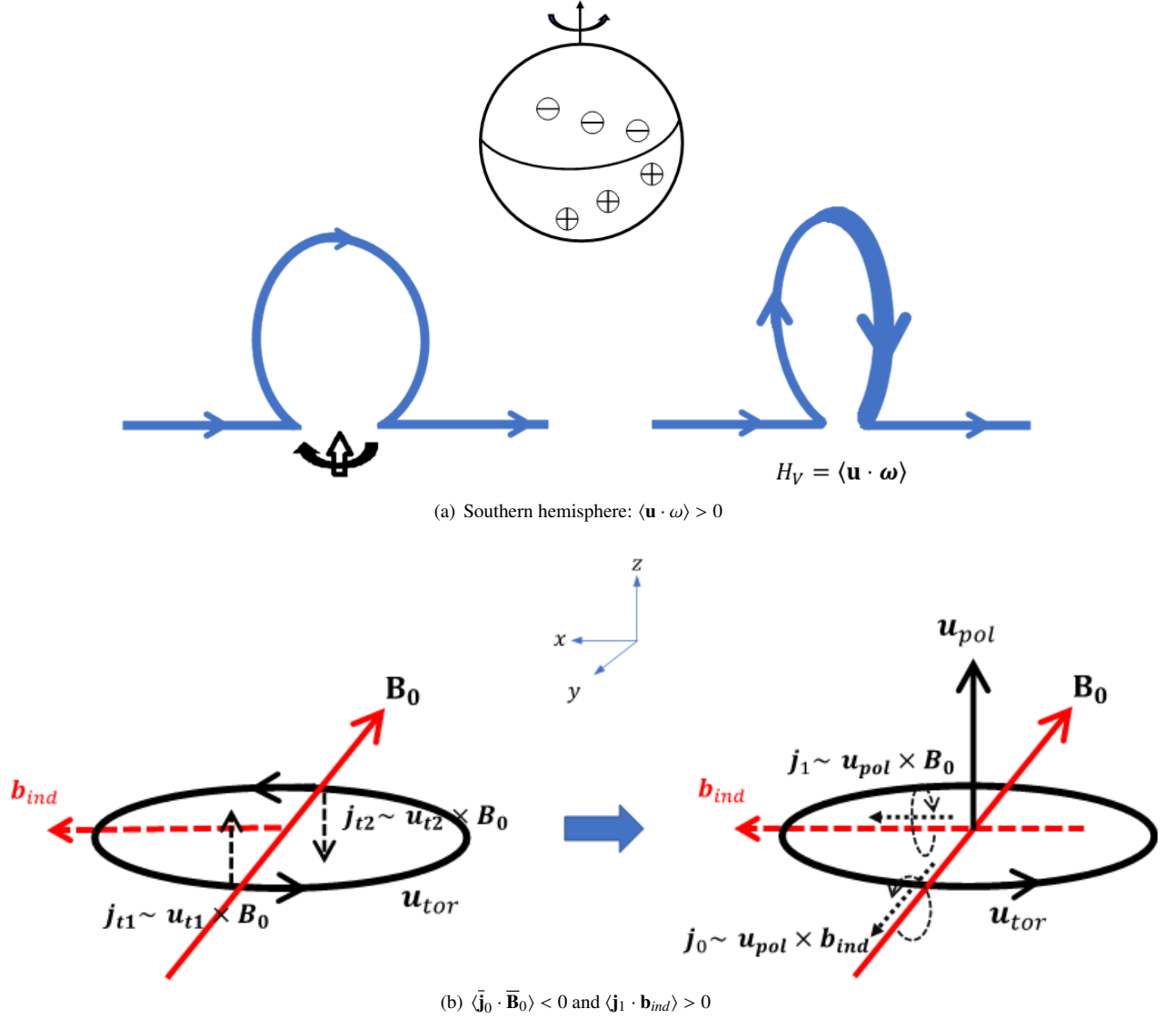
FIG. 2. (a) Right handed $\langle \mathbf{u} \cdot \omega \rangle$ in southern hemisphere. The plasma flux, buoyed toward the surface, is twisted clockwise by the Coriolis force, generating right-handed kinetic helicity as a result. (b) Induced left handed $\langle \bar{\mathbf{j}}_0 \cdot \overline{\mathbf{B}}_0 \rangle$ and right handed $\langle \mathbf{j}_1 \cdot \mathbf{b}_{ind} \rangle$ in the system driven by right handed $\langle \mathbf{u} \cdot \omega \rangle$. In the Northern Hemisphere, left-handed kinetic helicity is generated, leading to interactions with the magnetic field that exhibit opposite effects. Specifically, it can be expressed as $\langle \bar{\mathbf{j}}_0 \cdot \overline{\mathbf{B}}_0 \rangle > 0$ and $\langle \mathbf{j}_1 \cdot \mathbf{b}_{ind} \rangle < 0$ in northern hemisphere.

processes causing the uplift and twist (rotation) of $\mathbf{B}_{tor}$. In contrast, we focus on the electrodynamic aspect of the electromotive force (EMF), $\langle \mathbf{u} \times \mathbf{b} \rangle$, as the coupling coefficient of $\mathbf{B}_{tor}$ and $\mathbf{B}_{pol}$, addressing the limitations mentioned above. This approach becomes clear if we consider that the magnetic induction equation is derived from the electromagnetic effects, rather than being mechanically originated.

Our approach seeks to offer a more physically grounded explanation of the magnetic field generation processes by directly connecting the electromagnetic α effect, as it relates to current density, with observable solar magnetic field structures and dynamics.Specifically, we explore how the negative magnetic diffusion β effect, driven by helical turbulent plasma motions, contributes to the overall dynamo process. In particular, we aim to examine the similarities and differences in the α and β effects between the northern and southern hemispheres of a rotating astrophysical plasma sphere, such as the Sun. Following this, we plan to use the α and β values corresponding to each hemisphere to reproduce the large-scale magnetic field obtained from the simulations. However, it should be noted that the α and β values do not yet reflect the actual Reynolds number (Re, Re_M) and magnetic Prandtl number (Pr_M) of the Sun or other celestial system. Simulating these values for the Sun exceeds current computational capabilities, highlighting the need for more systematic studies on turbulence as a function of Reynolds numbers
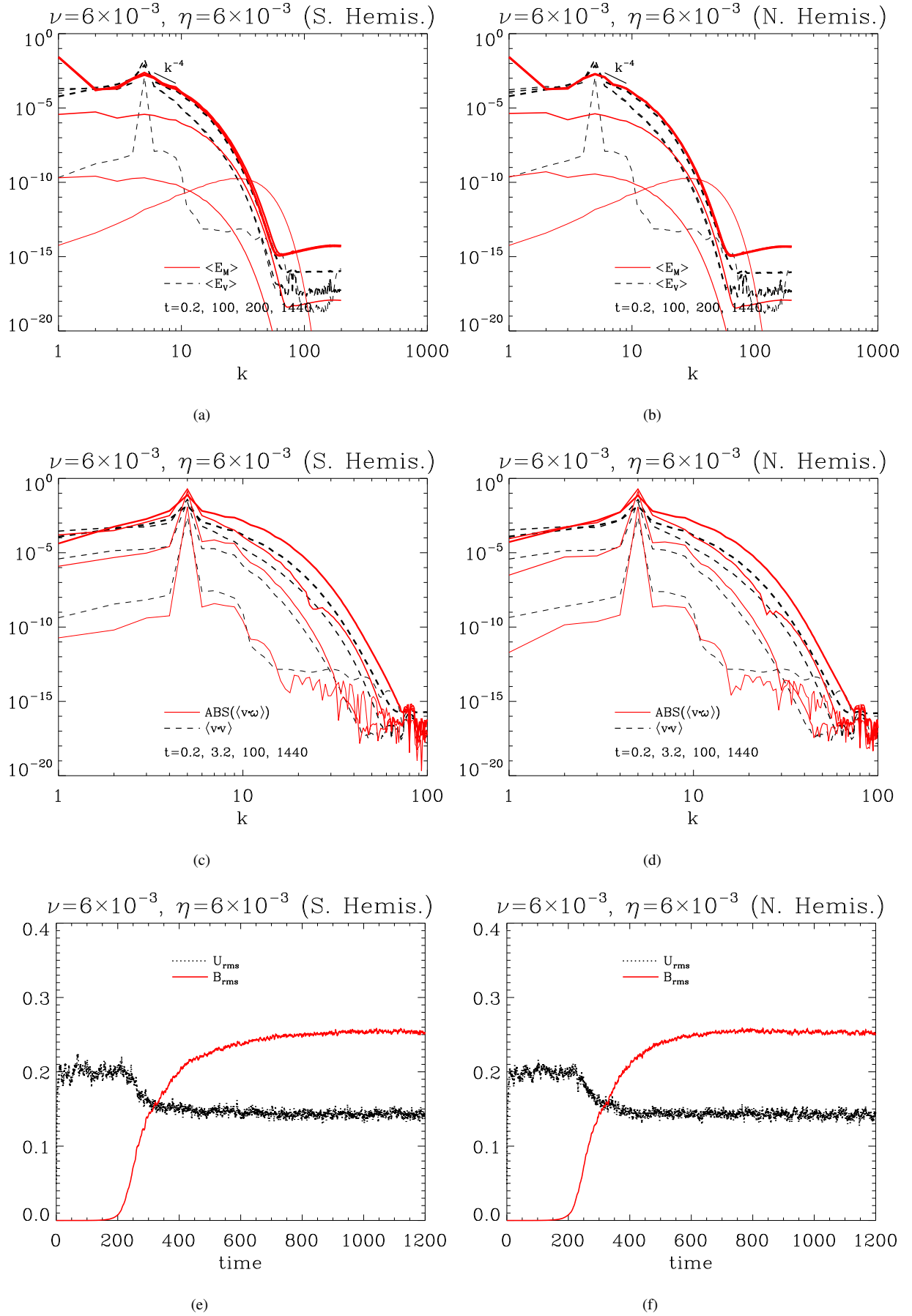
FIG. 3. Left panel: southern hemisphere (left handed kinetic helicity), right panel: northern hemisphere (right handed kinetic helicity).

(a)

(b)

(c) $|\langle \overline{\mathbf{A}} \cdot \overline{\mathbf{B}} \rangle|$ vs $\langle \overline{B}^2 \rangle$

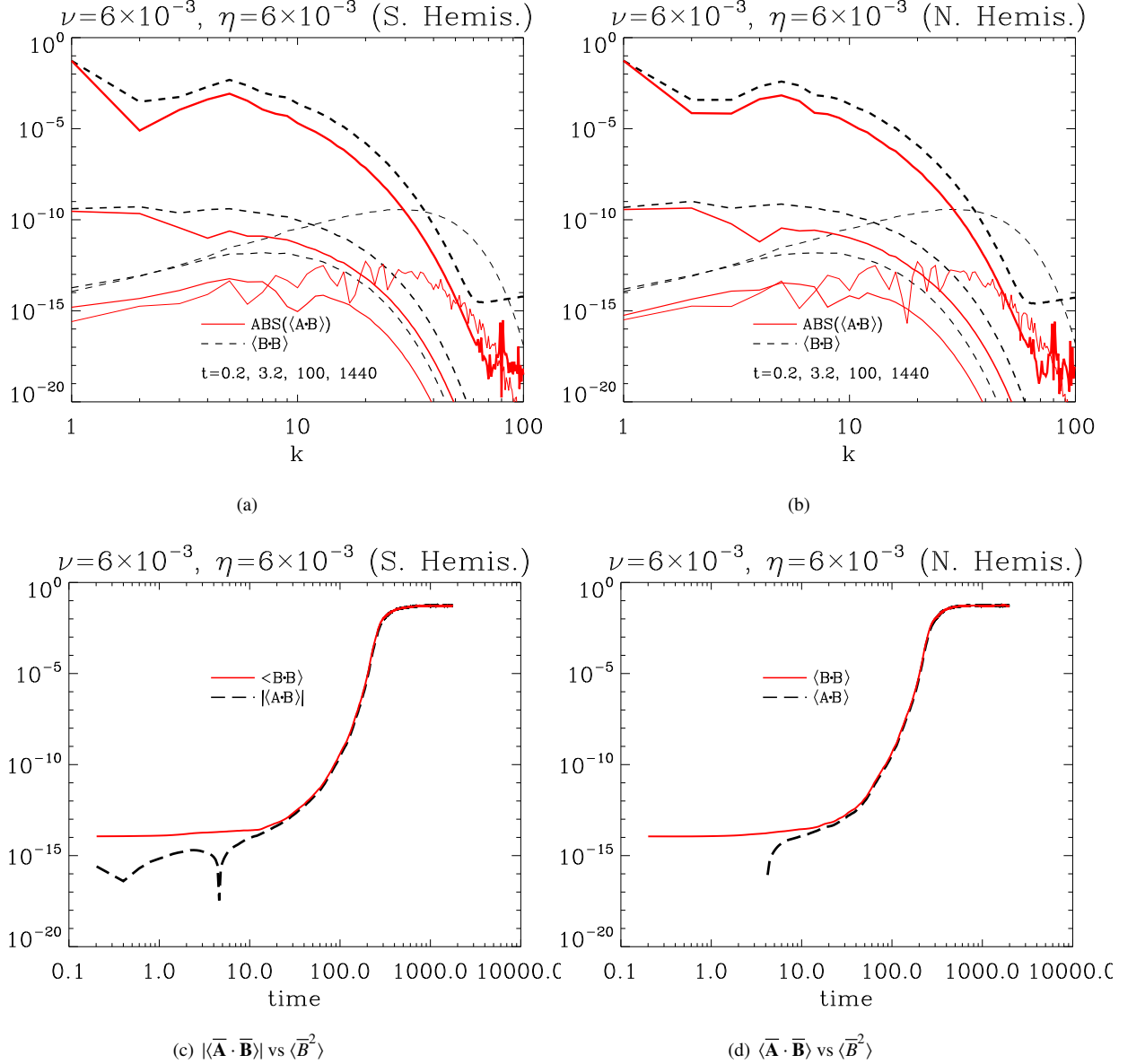(d) $\langle \overline{\mathbf{A}} \cdot \overline{\mathbf{B}} \rangle$ vs $\langle \overline{B}^2 \rangle$

FIG. 4. In the Southern Hemisphere, kinetic helicity has a positive value, resulting in the generation of magnetic helicity with a negative value, which is then transferred to larger scales. Therefore, the absolute value was used for comparison with the magnetic energy $\langle B^2 \rangle$. In contrast, in the Northern Hemisphere, helicity of the opposite polarity is generated, eliminating the need to use the absolute value. The difference between magnetic energy and magnetic helicity at large scales is used to determine $\alpha(t)$ and $\beta(t)$.

and magnetic Prandtl number. Therefore, for now, we limit our study to lower Re, Re_M, and $Pr_M = 1$ for a spherical rotating fluid system with oppositely polarized kinetic helicities in the Northern and Southern hemispheres. This perspective could provide a more useful understanding of magnetic activity within a rotating plasma system.

In our prior research [1, 15], we successfully derived $\alpha_{\text{EM-HM}}$ and $\beta_{\text{EM-HM}}$ from large-scale magnetic energy $\overline{E}_M (= \langle \overline{B}^2 \rangle / 2)$, and magnetic helicity $\overline{H}_M (= \langle \overline{A} \cdot \overline{B} \rangle, \ \overline{B} = \nabla \times \overline{A})$, without relying on any artificial assumptions or additional constraints on the system. By utilizing raw simulation data, we generated their profiles and successfully reproduced the evolving large-scale magnetic field, aligning with direct numerical simulations (DNS). Upon confirming that our model's outcomes were consistent with the DNS, we formulated additional expression for $\beta_{\text{VV-HV}}$, which necessitates turbulent kinetic energy $\langle u^2 \rangle / 2$ and helicity $\langle u \cdot \nabla \times u \rangle$. This new expression comprises two components: the conventional β effect and an additional term attributable to turbulent kinetic helicity. It is noteworthy that kinetic helicity influences not only the α effect but also the β effect. We generated profiles for $\alpha_{\text{EM-HM}}$ and $\beta_{\text{EM-HM}}$, as well as $\beta_{\text{VV-HV}}$, corresponding to positive and negative kinetic helicities, which pertain to
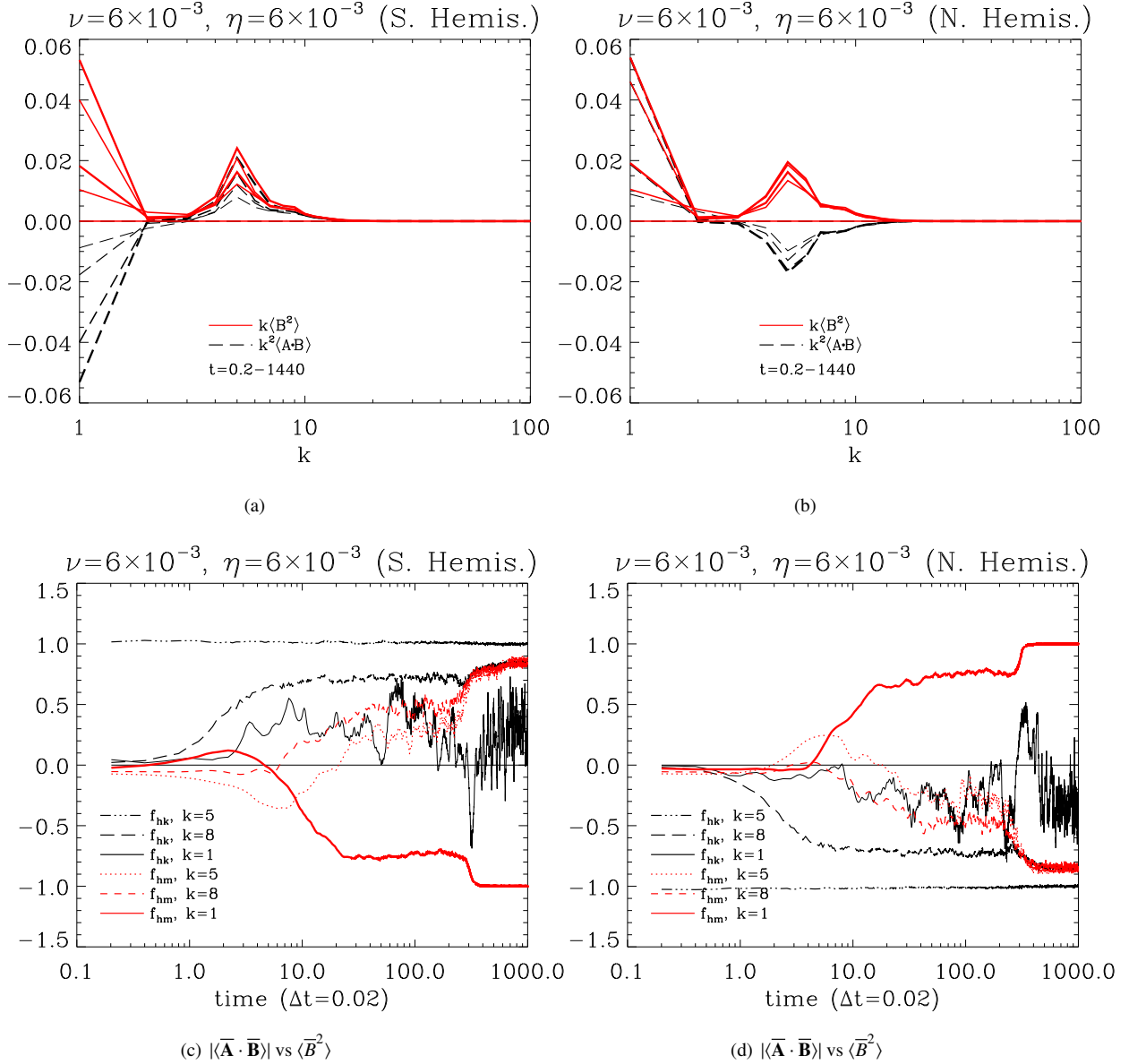
FIG. 5. In the turbulent region, the magnitude of magnetic helicity is too small, so current helicity was used for comparison. These two pseudoscalars ($\langle \overline{\mathbf{J}} \cdot \overline{\mathbf{B}} \rangle = \langle \overline{\mathbf{A}} \cdot \overline{\mathbf{B}} \rangle$) share similar physical properties and have the same value at the large scale with $k = 1$.

the Southern and Northern Hemispheres, respectively. Using these distinct datasets, we reconstructed the large-scale magnetic field $\overline{B}$. The comparisons between $\overline{B}_{DNS}$, $\overline{B}_{EM-HM}$, and $\overline{B}_{VV-HV}$ yield benchmarks that establish a framework for evaluating new methodologies.

This article is structured into five chapters. In the second chapter, we briefly discuss the general evolution of the magnetic field in a rotating spherical plasma system. Compared to Parker's or BL's models, this model is based on electromagnetic interactions within the magnetic induction equation. Poloidal magnetic fields, generated by current densities, and distorted toroidal magnetic fields give rise to oscillating helical magnetic structures. In the third chapter, we discuss the basic MHD dynamo theory for oppositely handed kinetic helicities from both spherical hemispheres. Some of these theoretical aspects have been addressed in our previous works; however, for consistency and readability, we reintroduce the relevant theories with appropriate citations. Additionally, for readers unfamiliar with this field, supplementary explanations have been included, along with detailed physical interpretations of the theoretical equations. The fourth chapter presents the simulation approach and numerical results, which are used to verify the theoretical findings. Using the α and β values obtained from theoretical results with MHD simulation data, we reproduce the large-scale magnetic field and compare it with the simulation results. Finally, the article concludes with a summary.
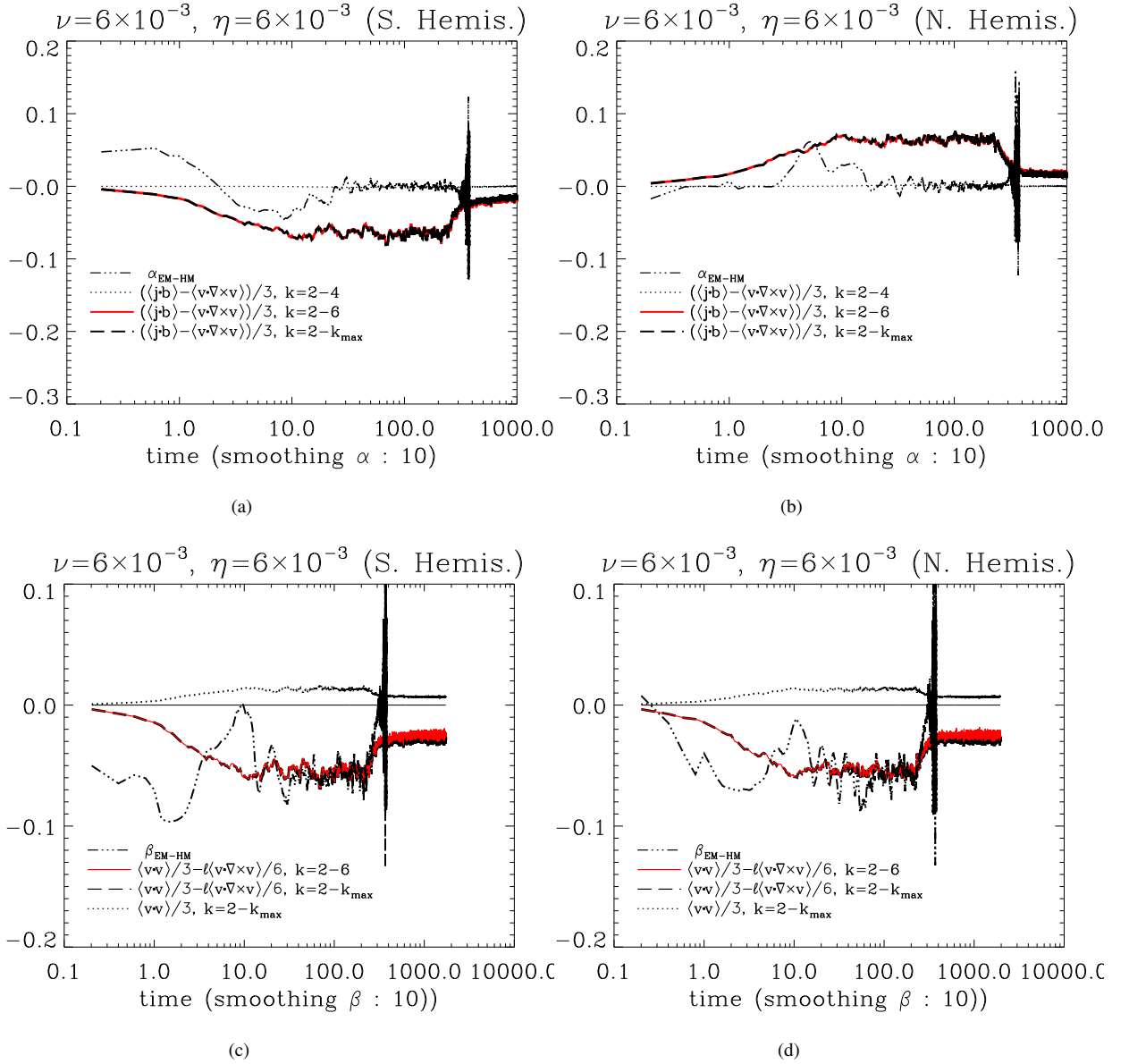
$\nu=6\times10^{-3}$, $\eta=6\times10^{-3}$ (S. Hemis.)

$\nu=6\times10^{-3}$, $\eta=6\times10^{-3}$ (N. Hemis.)

time (smoothing α : 10)

time (smoothing α : 10)

(a)

(b)

$\nu=6\times10^{-3}$, $\eta=6\times10^{-3}$ (S. Hemis.)

$\nu=6\times10^{-3}$, $\eta=6\times10^{-3}$ (N. Hemis.)

time (smoothing β : 10))

time (smoothing β : 10))

(c)

(d)

FIG. 6. For α & β, we applied a smoothing function in IDL, averaging over 10 nearby points.

II. OVERVIEW OF MAGNETIC EVOLUTION IN A ROTATING SPHERICAL SYSTEM

Figure 1 illustrates a model explaining the process of solar magnetic field formation. However, this model is not limited to the Sun or stars but can be applied to general rotating astrophysical plasma systems. Such systems consist of charged particles while maintaining overall electrical neutrality, with the Coriolis force present and buoyancy playing a significant role. Compared to other Solar models, we do not consider the poloidal magnetic field B_{pol} to be a result of the physical forces acting on the toroidal magnetic field B_{tor}. Instead, we believe that the current density J, generated parallel or antiparallel to B_{tor} due to kinetic helicity, contributes to the formation of B_{pol}. This reasoning is based on the physical interpretation of the electromotive force (EMF) in the magnetic induction equation, where the EMF moves charges, ultimately forming a current density, $-\mathbf{E} \sim \mathbf{U}\times\mathbf{B} \sim \mathbf{J}$.

In Figure 1(a), we assume that B_{pol}, flowing from north to south, is distorted by the sphere's differential rotation. This rotation then leads to the formation of (B_{tor}), which becomes most concentrated near the equator. Due to the Coriolis force and buoyancy
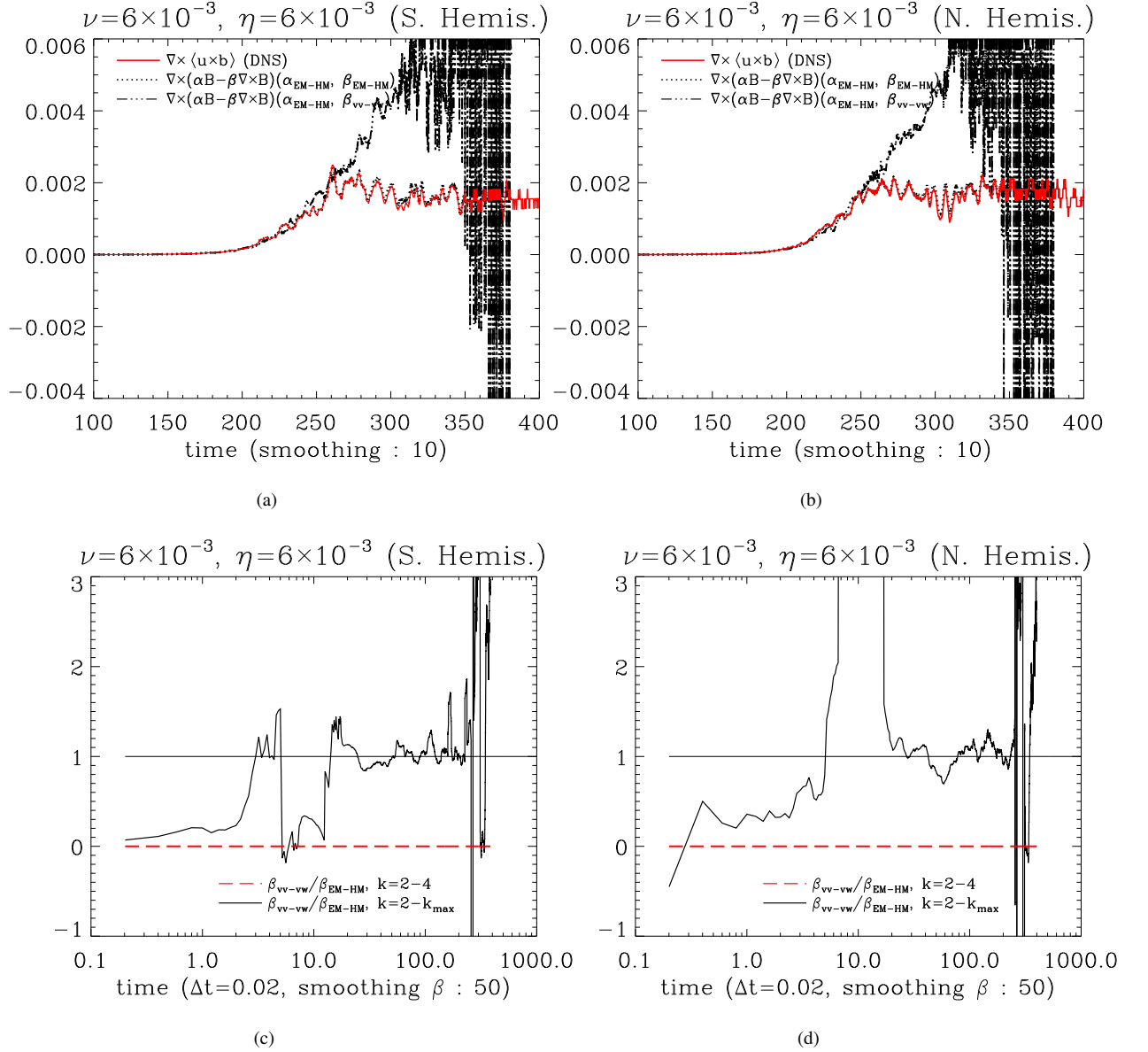
FIG. 7. Comparison of EMF by substituting α and β. $\alpha_{\text{EM-HM}}$ and $\beta_{\text{EM-HM}}$ are in good agreement with $\langle \mathbf{u} \times \mathbf{b} \rangle$. However, $\beta_{\text{VV-VW}}$ diverges from $t \sim 250$, which is due to the fact that the magnetic field effect is not reflected in Eq. (32).

in the rotating celestial body, left-handed (negative) kinetic helicity ($\langle \mathbf{u} \cdot \omega \rangle$, $\omega = \nabla \times \mathbf{u}$) is generated in the northern hemisphere, while right-handed (positive) kinetic helicity forms in the southern hemisphere. Kinetic helicity interacting with B_{tor} can induce J.

As Figure 1(b) shows, in the northern hemisphere, the current density (J) induced by left-handed kinetic helicity is in the same direction as the magnetic flux. On the contrary, (J) is induced in the opposite direction in the southern hemisphere. Due to the opposite direction of B_{tor} in both hemispheres, the current densities in the northern and southern hemispheres flow from west to east.

Figure 1(c) illustrates that these current densities, in turn, induce new magnetic fields (B_{pol0}). As a result, B_{tor} and B_{pol0} generate right-handed magnetic helicity in the northern hemisphere and left-handed magnetic helicity in the southern hemisphere. The fields B_{pol0} reconnect to form the poloidal field (B_{pol}).

In Figure 1(d), these small poloidal fields combine to form a large-scale B_{pol} that flows from the northern pole to the southern
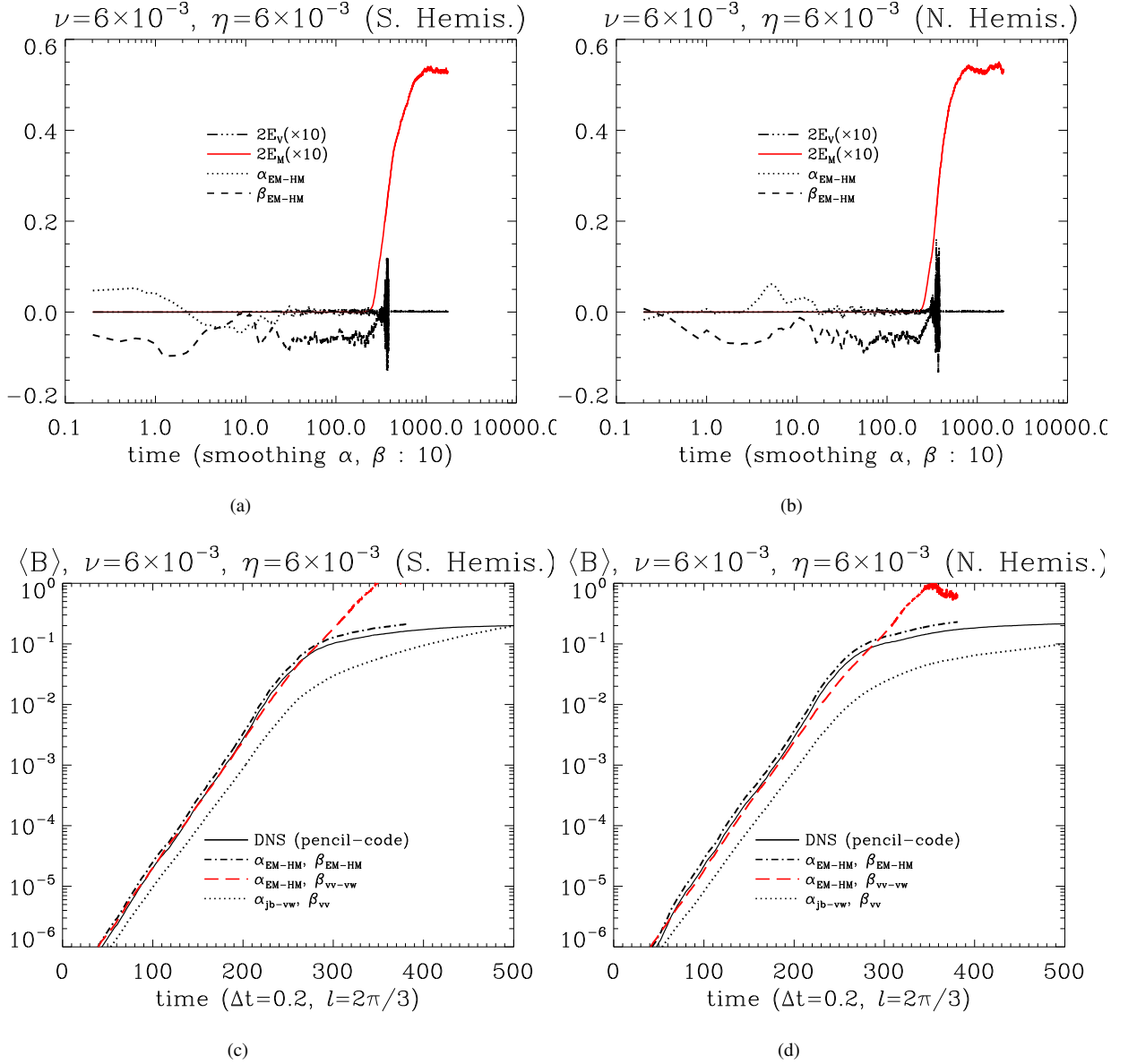
FIG. 8.

pole. It is important to note that the large-scale B_{pol} formed beneath B_{tor} flows in the opposite direction to B_{pol} above it, i.e., from south to north. This B_{pol} forms a new toroidal field (B_{tor2}) through differential rotation. However, B_{tor2} flows in the opposite direction to the original B_{tor}, as depicted in Figure 1(e). Meanwhile, the strongest B_{tor} near the solar surface has fewer or virtually no factors for further amplification compared to B_{tor2}, which is still influenced by differential rotation.

As B_{tor2} strengthens, the plasma density within the magnetic flux tube decreases, making it lighter and causing it to rise to the surface. There, it reconnects with the existing magnetic flux B_{tor}, canceling out the magnetic fields. The amplified, oppositely directed magnetic flux beneath the surface continues to rise, eventually reaching the surface and exhibiting reversed polarity, as shown in Figures 1(f) and 1(g). In the new cycle depicted in Figure 1(h), the current densities in both hemispheres flow from east to west, driven by the polarities of kinetic helicity. This process repeats every 11 years, accounting for the polarity reversal of the solar surface magnetic flux and the brief disappearance of magnetic fields between them.

$\nu = 6 \times 10^{-3}, \ \eta = 6 \times 10^{-3} \ (f_{hk} = 1 \to 0)$

(a) $2\overline{E} \ \& \ |\overline{H}_M|$

(b) f_{hk}, f_{hm} at $k = 1, 5, 8$

(c) α_{EM-HM} vs α_{MFT}

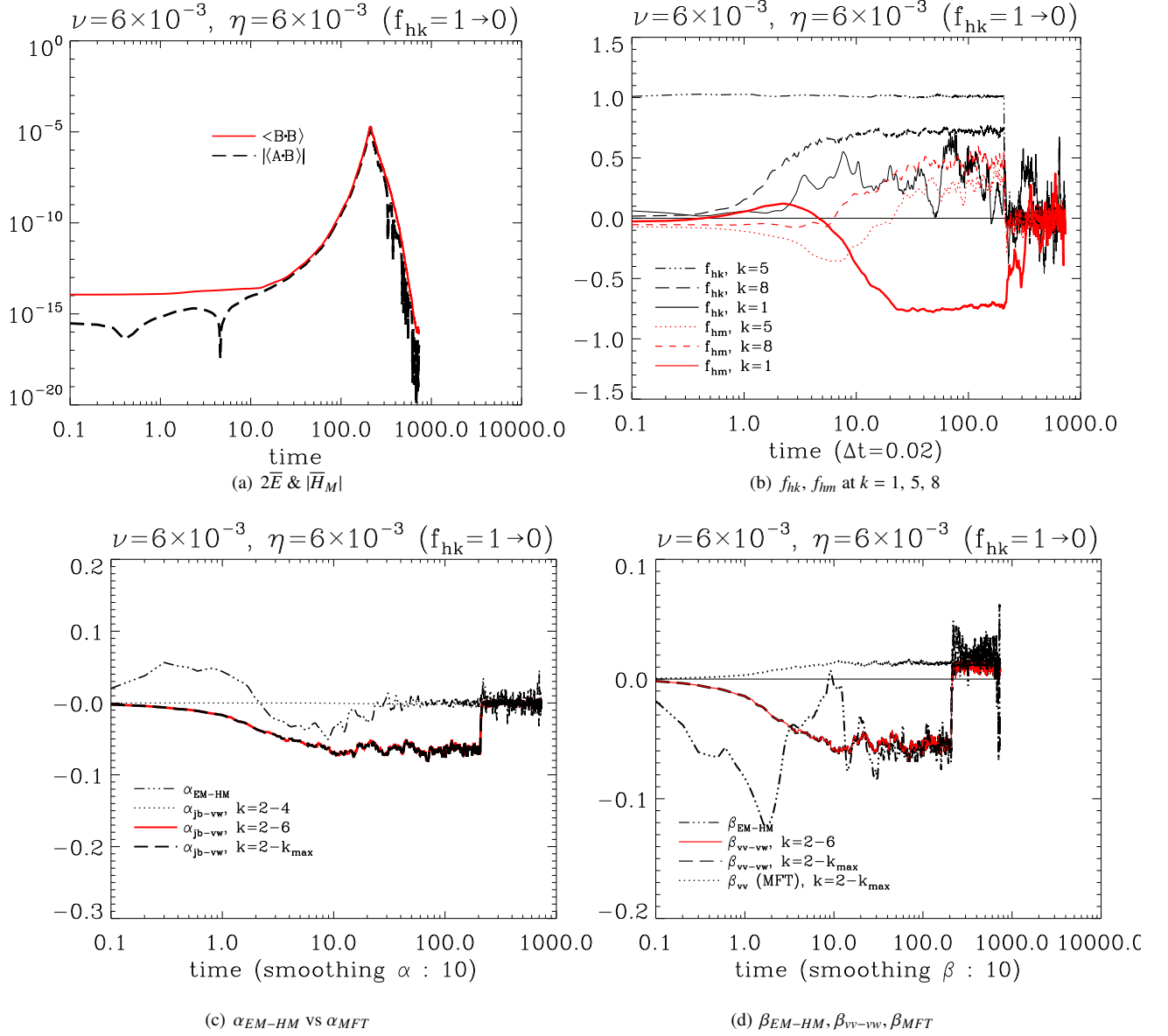(d) $\beta_{EM-HM}, \beta_{vv-vw}, \beta_{MFT}$

FIG. 9. The system was driven with positive kinetic helicity (Southern Hemisphere) and at $t = 210$, the helicity ratio was set to zero while maintaining the same energy: $\beta_{EM-HM} \sim \beta_{vv-vw} < \beta_{MFT} \to \beta_{EM-HM} \sim \beta_{vv-vw} \sim \beta_{MFT}$. (reproduced figures from [1])

III. BASIC MAGNETOHYDRODYNAMIC (MHD) EQUATIONS FOR SOLAR MAGNETIC FIELDS

The solar dynamo can be described by a set of nonlinear magnetohydrodynamic (MHD) equations that govern the dynamics of the electrically conducting magnetized plasma within the plasma systems.

$$\frac{D\rho}{Dt} = -\rho \nabla \cdot \mathbf{U}, \tag{1}$$

$$\frac{D\mathbf{U}}{Dt} = -\nabla \ln \rho + \frac{1}{\rho}(\nabla \times \mathbf{B}) \times \mathbf{B} + \nu\left(\nabla^2 \mathbf{U} + \frac{1}{3}\nabla\nabla \cdot \mathbf{U}\right) \tag{2}$$

$$\frac{\partial \mathbf{B}}{\partial t} = \nabla \times \langle \mathbf{U} \times \mathbf{B} \rangle + \eta \nabla^2 \mathbf{B} \tag{3}$$

Here, ρ, U, B, and $D/Dt(= \partial/\partial t + \mathbf{U} \cdot \nabla)$ indicate the density, velocity field, magnetic field, and Lagrangian time derivative in order. And ν & η are kinematic viscosity and magnetic diffusivity respectively.

These equations encapsulate the interactions between plasma flow, magnetic fields, and thermodynamic processes, providing a framework for understanding the generation and evolution of the density, velocity, and magnetic fields. The dynamo mechanism functions through the combined effects of differential rotation, convective motions, turbulent effects, diffusion, and internal or external forcing sources, leading to the amplification and regeneration of magnetic fields. These foundational equations are commonly applied in direct numerical simulations (DNS) or theoretical analyses. For computational studies, Eqs. (1)-(3) are solved using various numerical schemes [16]. For theoretical investigations, Eqs. (2) and (3) are typically solved with closure theories such as mean field theory (MFT; [17–19]), direct interaction approximation (DIA; [20]), and eddy-damped quasi-normal Markovian (EDQNM) approximation [21, 22]. Particularly when the fields in the system exhibit helicity, $\langle \mathbf{F} \cdot \nabla \times \mathbf{F} \rangle = \lambda \langle F^2 \rangle$, the magnetic induction equation [Eq. (3)] is modified (rederived) to include α and β coefficients, alongside the large-scale magnetic field $\overline{\mathbf{B}}$ and plasma velocity $\overline{\mathbf{U}}$.

$$
\begin{aligned}
\frac{\partial \overline{\mathbf{B}}}{\partial t} &= \nabla \times (\overline{\mathbf{U}} \times \overline{\mathbf{B}} + \langle \mathbf{u} \times \mathbf{b} \rangle) + \eta \nabla^2 \overline{\mathbf{B}} \\
&= \nabla \times (\overline{\mathbf{U}} \times \overline{\mathbf{B}} + \alpha \overline{\mathbf{B}} - \beta \nabla \times \overline{\mathbf{B}}) + \eta \nabla^2 \overline{\mathbf{B}}
\end{aligned}
\tag{4}
$$

Additionally, it is more convenient to express Eq. (4) in curvilinear coordinates [20, 23]:

$$
\frac{\partial \overline{\mathbf{A}}_\phi}{\partial t} + \frac{1}{\sigma} \overline{\mathbf{U}}_p \cdot \nabla(\sigma \overline{\mathbf{A}}_\phi) = \alpha \overline{\mathbf{B}}_\phi + (\beta + \eta) \left(\nabla^2 - \frac{1}{\sigma^2} \right) \overline{\mathbf{A}}_\phi,
\tag{5}
$$

$$
\frac{\partial \overline{\mathbf{B}}_\phi}{\partial t} + \sigma \overline{\mathbf{U}}_p \cdot \nabla \left(\frac{\overline{\mathbf{B}}_\phi}{\sigma} \right) = \alpha (\nabla \times \overline{\mathbf{B}}_p)_\phi + \sigma (\overline{\mathbf{B}}_p \cdot \nabla) \frac{\overline{\mathbf{U}}_\phi}{\sigma} + (\beta + \eta) \left(\nabla^2 - \frac{1}{\sigma^2} \right) \overline{\mathbf{B}}_\phi,
\tag{6}
$$

where $\overline{\mathbf{B}} = \overline{B}_\phi \hat{e}_\phi + \overline{\mathbf{B}}_p$, $\overline{\mathbf{B}}_p = \nabla \times (\overline{A}_\phi \hat{e}_\phi)$, and $\sigma = r \sin \theta$.

As indicated by Eqs. (4)-(6), the large-scale magnetic field $\overline{\mathbf{B}}$ cannot be sustained without the presence of α or β. The poloidal magnetic field and the toroidal component are coupled through the α effect, while both components can be influenced by β diffusion. Additionally, the toroidal field is driven by the shear of the differential rotation, $\nabla \overline{U}_\phi$. However, these three physical effects originate from different sources. $\nabla \overline{U}_\phi$ arises from the rotation of the spherical system, whereas α and β emerge from turbulent (helical) plasma motions and magnetic fields. Since the polarity of helicity is opposite in the Northern and Southern Hemispheres, it is necessary to examine how the α and β effects vary in each hemisphere and to verify whether the amplification of the magnetic field is consistent with theoretical predictions.

On the other hand, Eqa. (1)-(3) involve a combination of scalars, polar vectors, and axial vectors. In physics, it is not uncommon to encounter cases where different types of scalars and vectors are mixed within a single equation or concept. For example, the electromagnetic field tensor $F^{\mu\nu}$, which describes four-dimensional spacetime, includes both the electric field, a polar vector, and the magnetic field, an axial vector [24]. Similarly, the Lagrangian density uses both ordinary scalars and pseudo-scalars. Furthermore, Riemann solver $\partial \mathbf{U}/\partial t + \nabla \cdot \mathbf{F}(\mathbf{U}) = 0$ used for numerically solving MHD equations includes scalars, vectors, and axial vectors, simultaneously [16].

A.   Derivation of α & β

Several attempts have been made to calculate these coefficients using various dynamo theories such as MFT, EDQNM, and DIA. Despite these efforts, only approximations of the α and β coefficients are available. These theories suggest that α is related to residual helicity, $\langle \mathbf{b} \cdot (\nabla \times \mathbf{b}) \rangle - \langle \mathbf{u} \cdot (\nabla \times \mathbf{u}) \rangle$, while β is linked to turbulent energy, such as $\langle u^2 \rangle$ or $\langle b^2 \rangle$. Conventionally, α has been understood as a generator of magnetic fields, whereas β, in combination with molecular resistivity η, was thought to simply diffuse them. The theoretical expressions for α and β are outlined below.

(i) MFT [19, 25]:

$$
\alpha_{MFT} = \frac{1}{3} \int^\tau (\langle \mathbf{j} \cdot \mathbf{b} \rangle - \langle \mathbf{u} \cdot \nabla \times \mathbf{u} \rangle) \, dt,
\tag{7}
$$

$$
\beta_{MFT} = \frac{1}{3} \int^\tau \langle u^2 \rangle \, dt,
\tag{8}
$$

where τ is the correlation time, whose exact value remains unknown, isotropy is assumed, and higher-order terms are neglected.

(ii) DIA [20]:

$$\alpha_{DIA} = \frac{1}{3} \int d\mathbf{k} \int^t G\left(\langle \mathbf{j} \cdot \mathbf{b} \rangle - \langle \mathbf{u} \cdot \nabla \times \mathbf{u} \rangle\right) d\tau, \tag{9}$$

$$\beta_{DIA} = \frac{1}{3} \int d\mathbf{k} \int^t G\left(\langle u^2 \rangle + \langle b^2 \rangle\right) d\tau, \tag{10}$$

$$\gamma_{DIA} = \frac{1}{3} \int d\mathbf{k} \int^t G\langle \mathbf{u} \cdot \mathbf{b} \rangle\, d\tau, \tag{11}$$

Compared to MFD, the electromotive force (EMF) is characterized by the coefficients α, β, and γ, where γ represents cross helicity $\langle \mathbf{u} \cdot \mathbf{b} \rangle$. Additionally, β consists of contributions from both turbulent kinetic energy and magnetic energy. It should be noted that the dependence of β on magnetic energy cannot be derived through the function recursion approach.

(iii) EDQNM [22, 26]:

$$\alpha_{QN} = \frac{2}{3} \int^t \Theta_{kpq}(t)\left(\langle \mathbf{j} \cdot \mathbf{b} \rangle - \langle \mathbf{u} \cdot \nabla \times \mathbf{u} \rangle\right) dq, \tag{12}$$

$$\beta_{QN} = \frac{2}{3} \int^t \Theta_{kpq}(t)\langle u^2 \rangle\, dq, \tag{13}$$

The relaxation time Θ_{kpq} is given by $\frac{1-\exp(-\mu_{kpq}t)}{\mu_{kpq}}$, which converges to a constant over time: $\Theta_{kpq} \to \mu_{kpq}^{-1}$. The eddy damping operator μ_{kpq} is determined experimentally. Note that the coefficients α and β have a factor of 2/3, which stems from the quasi-normalization process that reduces fourth-order moments to second-order ones.

The EDQNM approach requires an additional time differentiation of the momentum and magnetic induction equations, resulting in fourth-order terms. In EDQNM, these fourth-order moments, $\langle x_l x_m x_n x_q \rangle$, are approximated by second-order moments under the assumptions of isotropy and homogeneity, i.e., $\sum_{lmnq}\langle x_l x_m \rangle\langle x_n x_q \rangle$. The second-order moments are then expressed in terms of E_V, E_M, H_V, H_M, and the cross helicity $\langle \mathbf{u} \cdot \mathbf{b} \rangle$. However, incorporating cross helicity into EDQNM requires more extensive theoretical calculations than the other terms, complicating the results. Typically, the EDQNM approach does not account for its effect, although it plays a role in decreasing the EMF $\langle \mathbf{u} \times \mathbf{b} \rangle$ dynamo effect.

(iv) Test field method [12]:
If the simulation with the artificial test field $\overline{B}^T$ is repeated, data sets for $\mathbf{u}$ and $\mathbf{b}$ can be obtained. Then, from

$$\xi_i = \langle \mathbf{u} \times \mathbf{b} \rangle_i = \alpha_{ij}\overline{B}^T_j + \beta_{ijk}\frac{\partial \overline{B}^T_j}{\partial x_k} + \gamma_{ijlk}\dots$$

the coefficients can be calculated. TFM provides detailed information on α_{ij} and β_{ijk} depending on the component and position [27, 28]. In particular, TFM reveals that the time-averaged magnetic diffusion effect, such as $\beta_{r\theta}$ and $\beta_{r\phi}$, is effectively negative, which is consistent with the negative β effect observed in our study [27, 29, 30]. However, the validity of $\overline{B}^T$ still requires further consideration. When the test magnetic field is applied, charged particles move freely along the direction of $\overline{B}^T$, while their motion perpendicular to $\overline{B}^T$ is constrained by the field. As $\overline{B}^T$ increases, the Larmor radii of the particles shrink, and the electric Coulomb interactions, along with the binding energy between the particles, are altered. This leads to a particle distribution geometry resembling a needle shape. As a result, the distribution function f becomes anisotropic, requiring the continuity and momentum equations to be split into parallel and perpendicular components. The anisotropic nature introduced by the external $\overline{B}^T$ field cannot be disregarded. Of course, as assumed in TFM, if the size of the test field is very small, the impact on the distribution function will be limited. Nonetheless, it is still uncertain whether such a hypothetical field can be applied to actual observations.

B. Alternative Derivation of α and β using large scale magnetic data

As pointed out, MFT neglects higher-order terms and cannot self consistently determine the eddy turnover time τ, while DIA cannot determine τ and the Green function G. Similarly, EDQNM struggles with calculating τ, Θ_{kpq}, μ_{kpq}, and moments of

order higher than four. Furthermore, each of these methods develops its theoretical framework based on assumptions of homogeneity and isotropy; thus, as magnetic field strength and anisotropy increase, errors also grow. Considering these limitations in MHD dynamo theory, we devised a method to calculate α and β using the large-scale or mean magnetic helicity $\overline{H}_M$ and magnetic energy $\overline{E}_M$, which are physically conserved quantities. We have previously utilized and advanced this model in our works [1, 15, 31]. However, for the sake of consistency and readability, we provide a more detailed basic explanation of the theoretical process previously employed, rather than simply referencing it. It is essential to articulate the underlying concepts and derivations when applying this methodology to real data or Direct Numerical Simulations (DNS).

From Eq. (4), we derive the coupled equations for $\overline{H}_M(t)$ and $\overline{E}_M(t)$ as follows:

$$\frac{\partial \overline{H}_M}{\partial t} = 4\alpha \overline{E}_M - 2(\beta + \eta)\overline{H}_M, \tag{14}$$

$$\frac{\partial \overline{E}_M}{\partial t} = \alpha \overline{H}_M - 2(\beta + \eta)\overline{E}_M. \tag{15}$$

Here, we use the relationships $\overline{\nabla} \times \overline{\mathbf{A}} = \overline{\mathbf{B}} = \lambda_1 \overline{\mathbf{A}}$ and $\overline{\nabla} \times \overline{\mathbf{B}} = \overline{\mathbf{J}} = \lambda_2 \overline{\mathbf{B}}$, along with the assumption that the curl operator for large-scale fields does not affect small-scale quantities: $\overline{\nabla} \times \alpha \overline{\mathbf{B}} = \alpha \overline{\nabla} \times \overline{\mathbf{B}}$. And, for the large scale field with $k = 1$, magnetic helicity and current helicity coincide: $\langle \mathbf{J} \cdot \mathbf{B} \rangle = k^2 \langle \mathbf{A} \cdot \mathbf{B} \rangle \rightarrow \langle \mathbf{A} \cdot \mathbf{B} \rangle$. Also, note that the wavenumber k, which is inversely proportional to the eddy scale $\sim 1/l$, is relative depending on the system's dimension.

Then, we apply Gauss's law with the vanishing integral in the infinite limit:

$$\int \nabla \cdot \left[\overline{\mathbf{A}} \times (\overline{\mathbf{U}} \times \overline{\mathbf{B}}) \right] dV = \int^\infty \left[\overline{\mathbf{A}} \times (\overline{\mathbf{U}} \times \overline{\mathbf{B}}) \right] \cdot \hat{\mathbf{n}} \, dS = 0.$$

Additionally, we considered the substitution $\nabla \rightarrow ik$ with $k = 1$ for large-scale fields. These coupled differential equations can be solved using standard methods:

$$\begin{bmatrix} \partial \overline{H}_M / \partial t \\ \partial \overline{E}_M / \partial t \end{bmatrix} = \begin{bmatrix} -2(\beta + \eta) & 4\alpha \\ \alpha & -2(\beta + \eta) \end{bmatrix} \begin{bmatrix} \overline{H}_M \\ \overline{E}_M \end{bmatrix} = \begin{bmatrix} \lambda & 0 \\ 0 & \lambda \end{bmatrix} \begin{bmatrix} \overline{H}_M \\ \overline{E}_M \end{bmatrix}, \tag{16}$$

$$\Rightarrow \lambda_{1,2} = \pm 2\alpha - 2(\beta + \eta), \quad \texttt{eigen vector } X = \frac{1}{\sqrt{5}} \begin{bmatrix} 2 & 2 \\ 1 & -1 \end{bmatrix} \tag{17}$$

The solutions are

$$2\overline{H}_M(t) = (2\overline{E}_{M0} + \overline{H}_{M0})e^{2\int_0^t (\alpha - \beta - \eta)d\tau} - (2\overline{E}_{M0} - \overline{H}_{M0})e^{2\int_0^t (-\alpha - \beta - \eta)d\tau}, \tag{18}$$

$$4\overline{E}_M(t) = (2\overline{E}_{M0} + \overline{H}_{M0})e^{2\int_0^t (\alpha - \beta - \eta)d\tau} + (2\overline{E}_{M0} - \overline{H}_{M0})e^{2\int_0^t (-\alpha - \beta - \eta)d\tau}. \tag{19}$$

These solutions adhere to the realizability criterion $2\overline{E}_M > \overline{H}_M$. For the case where right-handed helical kinetic forcing is applied in the Southern Hemisphere, $\alpha \sim (\langle \mathbf{j} \cdot \mathbf{b} \rangle - \langle \mathbf{u} \cdot \omega \rangle)$ remains negative until $\langle \mathbf{j} \cdot \mathbf{b} \rangle$ reaches a sufficiently large value. Under these conditions, the second terms in each solution become dominant, resulting in $2\overline{H}_M(t) = -(2\overline{E}_{M0} - \overline{H}_{M0})e^{2\int_0^t (-\alpha - \beta - \eta)\,d\tau}$ and $4\overline{E}_M(t) = (2\overline{E}_{M0} - \overline{H}_{M0})e^{2\int_0^t (-\alpha - \beta - \eta)\,d\tau}$. Consequently, the large-scale magnetic helicity ratio approaches $\overline{f}_h = \overline{H}_M(t)/2\overline{E}_M(t) \rightarrow -1$. This result aligns with the values of f_{hm} at $k = 1$ shown in Figures 6(a) and 6(c). Conversely, in the Northern Hemisphere with right-handed helical kinetic energy, f_{hm} at $k = 1$ approaches $+1$, as illustrated in Figures 6(b) and 6(d).

The coefficients α and β can be determined directly. By multiplying Eq. (15) by 2 and subtracting it from Eq. (14), we obtain an expression for $\overline{H}_M - 2\overline{E}_M$. Alternatively, summing these two equations yields a formula for $\overline{H}_M + 2\overline{E}_M$. Using these results, we can derive the required expressions as follows:

$$\alpha(t) = \frac{1}{4}\frac{d}{dt}log_e \left| \frac{2\overline{E}_M(t) + \overline{H}_M(t)}{2\overline{E}_M(t) - \overline{H}_M(t)} \right|, \tag{20}$$

$$\beta(t) = -\frac{1}{4}\frac{d}{dt}log_e \left| (2\overline{E}_M(t) - \overline{H}_M(t))(2\overline{E}_M(t) + \overline{H}_M(t)) \right| - \eta. \tag{21}$$

Substituting this result into Eq. (14) and Eq. (15) confirms equality between the left and right sides. Note that α and β are functions of large-scale magnetic data expressed in differential form rather than integral form. This approach, along with the use of differentiation, enhances the accuracy of the calculations.

Verification of these results with numerically simulated data is necessary before applying them to real-world data. To generate the desired profiles, we require a data set of $\overline{E}_M(t)$ and $\overline{H}_M(t)$ obtained from direct numerical simulations (DNS) at specified time intervals. We utilized an approximation such as

$$\frac{\partial F}{\partial t} \sim \frac{\Delta F}{\Delta t} \sim \frac{F(t_n) - F(t_{n-1})}{t_n - t_{n-1}}.$$

The IDL script for α & β is as follows:

```
for j=0L,  i_last-1 do begin
    c[j]=2.0*spec_mag(1, j) + spechel_mag(1, j)     % k=1 for large scale
    d[j]=2.0*spec_mag(1, j) - spechel_mag(1, j)
endfor


for j=0L,  i_last-1 do begin
  alpha[j]= 0.25*((ALOG(c[j+1])-ALOG(c[j]))-(ALOG(d[j+1])-ALOG(d[j])))/(time[j+1]-time[j])
  beta[j] =-0.25*((ALOG(c[j+1])-ALOG(c[j]))+(ALOG(d[j+1])-ALOG(d[j])))/(time[j+1]-time[j])-eta
endfor
```

`ALOG( )` denotes the logarithmic function that returns the natural logarithm of `X`. `spec_mag( )` and `spechel_mag( )` represent arrays of power spectrum data for large scale magnetic energy $\langle \overline{B}^2 \rangle/2$ and magnetic helicity $\langle \overline{\mathbf{A}} \cdot \overline{\mathbf{B}} \rangle$, respectively, as obtained from Eqs. (1)-(3). DNS data was used here, but observational data can be used as well.

C.   Derivation of β using turbulent kinetic data

With Eqs. (20) and (21), the profiles of α and β can be determined exactly. However, this indirect approach does not explain the physical mechanisms by which these effects are formed. Therefore, we rederive β again using the function iterative approach, with a more detailed statistical identity relation. Conventionally, β is found with

$$\left\langle \mathbf{u} \times \int^{\tau} (-\mathbf{u} \cdot \nabla \overline{\mathbf{B}}) dt \right\rangle \sim \left\langle -\epsilon_{ijk} u_j(r) u_m(r+l) \tau \frac{\partial \overline{B}_k}{\partial \overline{r}_m} \right\rangle \rightarrow -\frac{\tau}{3} \langle u^2 \rangle \epsilon_{ijk} \frac{\partial \overline{B}_k}{\partial \overline{r}_m} \delta_{jm}. \tag{22}$$

The eddy turnover time τ can be set as 1 under the assumption that the two eddies u_j and u_m are correlated over one eddy turnover time. However, assuming the spatial correlation length 'l' for u_j and u_m to be $l \rightarrow 0$ and replacing the second-order velocity moment with kinetic energy is overly simplified. Here, we introduce the methods used in our previous works applying a more general identity for the second-order moment as follows ([1], references therein):

$$U_{jm} \equiv \langle u_j(r) u_m(r+l) \rangle = A(l)\delta_{jm} + B(l)l_j l_m + C(l)\epsilon_{jms} l_s. \tag{23}$$

With $\vec{l} = (l, 0, 0)$ or other appropriate coordinates, we infer the relation of 'A', 'B', and 'C' as follows: $A + l^2 B \equiv F$, $A \equiv G$, $(U_{23} =)lC \equiv H$. Then, Eq.(23) is represented as

$$U_{jm} = G\delta_{jm} + \frac{(F-G)}{l^2} l_j l_m + H\epsilon_{jms}\frac{l_s}{l}. \tag{24}$$

With $\nabla \cdot \mathbf{U} = 0$, we get the additional constraint.

$$\frac{\partial U_{jm}}{\partial l_j} = \frac{l_j}{l} G' \delta_{jm} + 4l_m \frac{F-G}{l^2} + l_m \frac{(F'-G')l^2 - 2l(F-G)}{l^3} = 0, \tag{25}$$

which leads to $G = F + (l/2)\,\partial F/\partial l$. So, the second order moment is

$$U_{jm} = \left(F + \frac{l}{2}\frac{\partial F}{\partial l} \right)\delta_{jm} - \frac{l}{2l^2}\frac{\partial F}{\partial l} l_j l_m + H\epsilon_{jms}\frac{l_s}{l}. \tag{26}$$

If $j = m$, then $U_{jj} = F = u^2/3 = E_V/6$. Conversely, if $j \neq m$, the relation

$$\left\langle \epsilon_{ijk} u_j(r) u_m(r+l) \frac{\partial \overline{B}_k}{\partial \overline{r}_m} \right\rangle \rightarrow -\left\langle \frac{\epsilon_{ijk} l_j l_m}{2l}\frac{\partial F}{\partial l} \right\rangle \frac{\partial \overline{B}_k}{\partial \overline{r}_m}$$

indicates that any value of m renders the average negligible. For the term H, we utilize Lesieur's approach [32]:

$$
\begin{aligned}
H_V &= \lim_{y \to x} \mathbf{u}(\mathbf{x}) \cdot \nabla \times \mathbf{u}(\mathbf{y}) \\
&= \lim_{y \to x} \epsilon_{ijn} u_i \frac{\partial u_n}{\partial y_j} = \lim_{l \to 0} \epsilon_{ijn} \frac{\partial U_{in}(l)}{\partial l_j} \quad (\leftarrow y = x + l) \\
&= \lim_{l \to 0} \epsilon_{ijn} \epsilon_{ins} \left(\delta_{js} \frac{H}{l} - \frac{l_j l_s}{l^3} H + \frac{l_j l_s}{l^2} \frac{\partial H}{\partial l} \right) = -\frac{6}{l} H
\end{aligned}
\tag{27}
$$

Then, U_{jm} is

$$
U_{jm} = \frac{\langle u^2 \rangle}{3} \delta_{jm} - \epsilon_{jms} \frac{l_s}{6} H_V.
\tag{28}
$$

EMF by the advection term $-\mathbf{u} \cdot \nabla \overline{\mathbf{B}}$ can be represented as follows:

$$
\begin{aligned}
\left\langle -\epsilon_{ijk} u_j(r) u_m(r+l) \frac{\partial \overline{B}_k}{\partial \overline{r}_m} \right\rangle &= -\frac{1}{3} \langle u^2 \rangle \epsilon_{ijk} \frac{\partial \overline{B}_k}{\partial \overline{r}_m} \delta_{jm} + \epsilon_{ijk} \epsilon_{jms} \frac{l_s}{6} H_V \frac{\partial \overline{B}_k}{\partial \overline{r}_m} \\
&\Rightarrow -\frac{1}{3} \langle u^2 \rangle \nabla \times \overline{\mathbf{B}} + \frac{l}{6} H_V (\nabla \times \overline{\mathbf{B}})
\end{aligned}
\tag{29}
$$

For the second term in RHS, we referred to vector identity $\epsilon_{ijk} \epsilon_{jms} = \delta_{km} \delta_{is} - \delta_{ks} \delta_{im} \to -\delta_{ks} \delta_{im}$ with $\nabla \cdot \overline{\mathbf{B}} = 0$.

$$
\left\langle \epsilon_{ijk} \epsilon_{jms} \frac{l_s}{6} H_V \frac{\partial \overline{B}_k}{\partial \overline{r}_m} \right\rangle \to \left\langle \epsilon_{jik} \frac{l}{6} H_V \right\rangle \epsilon_{ijk} \frac{\partial \overline{B}_k}{\partial \overline{r}_i} \to \frac{l}{6} H_V (\nabla \times \overline{\mathbf{B}})_j.
\tag{30}
$$

We used the normal permutation rule and regarded l_s as l. Finally,

$$
\left(\frac{1}{3} \langle u^2 \rangle - \frac{l}{6} H_V \right) (-\nabla \times \overline{\mathbf{B}}) \equiv \beta (-\nabla \times \overline{\mathbf{B}}).
\tag{31}
$$

Now, we can set β_{VV-HV} as

$$
\beta_{VV-HV} = \frac{1}{3} \langle u^2 \rangle - \frac{l}{6} \langle \mathbf{u} \cdot \nabla \times \mathbf{u} \rangle = \frac{2}{3} E_V - \frac{l}{6} H_V.
\tag{32}
$$

Here, H_V is a pseudoscalar, and E_V is a scalar. Therefore, if we reflect them across a mirror at the origin ($l \to -l$), H_V changes its sign, while E_V remains unchanged. However, $l/6 H_V$ itself retains the same value (scalar) under mirror symmetry, just as $\langle u(r) u(r+l) \rangle = \langle u(r-l) u(r) \rangle$. Also, as mentioned, the simultaneous use of different types of scalars and vectors within the same theory or equation is not forbidden in principle. Furthermore, setting $l \to 0$ is a convenient assumption made for limiting the energy term from the second moment, and it is not necessary to strictly follow the $l \to 0$ case in MHD models. MHD is a model that describes phenomena formed by interactions with other eddies, and it does not make sense to restrict MHD phenomena to the case of $l = 0$. In other words, the meaning of the averaging used when deriving the MHD model from the Boltzmann equation does not constrain l.

D. The Role of Kinetic Helicity in Magnetic Field Amplification via α and β Effects

It is necessary to understand the generation of kinetic helicity due to the Coriolis force and buoyancy in a rotating plasma sphere, and how the generated helicity interacts with the seed magnetic field to produce a magnetic field. All these processes are inferred based on the physical and mathematical characteristics of each term in the magnetic induction equation.

Figure 2(a) shows the kinetic helicity generated in a rotating plasma sphere. In the solar convection zone ($0.7R_\odot - 1.0R_\odot$), numerous tube-shaped plasma flux structures exist. The plasma inside the tube is pushed outward due to the balance between magnetic pressure and thermal pressure, making it relatively lighter than the surrounding medium and causing it to rise toward the solar surface. During this process, a portion of the plasma eddy stretches, reducing its density further and increasing its buoyancy, which leads to the deformation of the tube structure. At this stage, the Coriolis force causes the circular loop to rotate in a clockwise direction, generating right-handed kinetic helicity in the Southern Hemisphere. Conversely, in the Northern Hemisphere, left-handed kinetic helicity is generated. This kinetic helicity interacts with the magnetic field, inducing new

magnetic fields (opposite polarity), as illustrated in Figure 2(b).

In Figure 2(b), the left panel illustrates a circular structure of a plasma turbulence eddy through which a magnetic field, $\mathbf{B}_0$, permeates, influencing both the eddy's structure and energy distribution. Plasma motions, labeled $\mathbf{u}_{t1}$ and $\mathbf{u}_{t2}$, interact with $\mathbf{B}_0$ to produce current densities, $\mathbf{j}_{t1}(\hat{z})$ and $\mathbf{j}_{t2}(-\hat{z})$. According to Ampère's law, these current densities induce a magnetic field, $\mathbf{b}_{\mathrm{ind}}(\hat{x})$, creating magnetic diffusion through the relationship $\nabla \times \mathbf{j}_t = \nabla \times (\nabla \times \mathbf{b}_{\mathrm{ind}}) = -\nabla^2 \mathbf{b}_{\mathrm{ind}}$. This newly induced magnetic field interacts with the plasma eddies to generate another magnetic field. This process of magnetic field induction occurs continuously, ultimately leading to the weakening of the original magnetic field. These sequential processes explain the magnetic diffusion β effect due to plasma turbulence fluctuations $\beta \sim \int \langle u^2 \rangle d\tau$.

However, when the velocity field has a helical component, as shown in the right panel, an additional poloidal velocity component $\mathbf{u}_{\mathrm{pol}}$ appears. This component interacts with $\mathbf{b}_{\mathrm{ind}}$ to create a current density $\mathbf{u}_{pol} \times \mathbf{b}_{ind} \sim \mathbf{j}_0(\hat{y})$, which in turn induces a toroidal magnetic field $\mathbf{b}_{\mathrm{tor}}$. $\mathbf{B}_0$ (acting as a poloidal field) and $\mathbf{b}_{\mathrm{tor}}$ form left-handed magnetic helicity, H_{M1}. Simultaneously, $\mathbf{u}_{\mathrm{pol}}$ can interact with $\mathbf{B}_0$ to produce another current density, $\mathbf{j}_1$, with $\mathbf{b}_{\mathrm{ind}}$ and $\mathbf{j}_1$ forming right-handed magnetic helicity, H_{M2} (see Figs. 5(a)-5(d)).

In this figure, $\mathbf{B}_0$, $\mathbf{u}_{\mathrm{pol}}$, and $\mathbf{b}_{\mathrm{ind}}$ are depicted as intersecting at the same point. However, while $\mathbf{b}_{\mathrm{ind}}$ and $\mathbf{u}_{\mathrm{pol}}$ intersect each other, $\mathbf{B}_0$ and $\mathbf{u}_{\mathrm{pol}}$ can be separated. Consequently, j_0 is greater than j_1. Then, H_{M1} may be interpreted as the magnetic helicity generated by kinetic helicity and transferred inversely to larger scales. In contrast, H_{M2} can be understood as the magnetic helicity produced to conserve the total magnetic helicity within the system. This reasoning aligns with the theoretical prediction that kinetic helicity generates magnetic helicity of opposite polarity, which is then amplified and transferred to larger scales, while magnetic helicity of the same polarity is generated in the small-scale region. This model, of course, does not exactly match the theoretical calculations. However, it demonstrates the mechanism of magnetic amplification in a helical plasma system and magnetic diffusion in a nonhelical plasma system. The α effect arises fundamentally from the interaction between the induced current density and the magnetic field, both of which originate from the diffusion of the seed magnetic field, β effect.

IV. NUMERICAL APPROACH

The theoretical results can be applied to DNS or observational data to determine α and β. In this section, we discuss the physical characteristics of a right-handed plasma system and a left-handed one, representing both hemispheres in a rotating astrophysical system. We then present the profiles of α and β obtained using Eqs. (20) and (21), and verify these results through various methods.

A. Numerical Method

We used the PENCIL CODE to perform our numerical simulations. This code solves Eqs. (1)-(3) within a periodic cube of size $(2\pi)^3$, discretized into a grid of 400^3 points. The velocity and magnetic fields are scaled by the sound speed, c_s, and $(\rho_0 \mu_0)^{1/2} c_s$, respectively. These scalings follow from the relations $E_M \sim B^2/\mu_0$ and $E_V \sim \rho_0 U^2$, where μ_0 and ρ_0 represent the magnetic permeability of free space and the initial density. It's worth noting that the plasma system is weakly compressible, meaning $\rho \sim \rho_0$. The system is forced with $\mathbf{f}_{kin}(x,t) = N \mathbf{f}(t) \exp\left[i \mathbf{k}_f(t) \cdot \mathbf{x} + i\phi(t)\right]$, which is attached to the momentum equation Eq. (2). N is a normalization factor, $\mathbf{f}(t)$ is the forcing magnitude, and $\mathbf{k}_f(t)$ represents the forcing wave number. At each time step, the code randomly selects one of 20 vectors from the $\mathbf{k}_f$ set. For simplicity, we set c_s, μ_0, and ρ_0 to 1, making the equations dimensionless.

The forcing function $\mathbf{f}(t)$ is defined as $f_0 \mathbf{f}_k(t)$:

$$\mathbf{f}_k(t) = \frac{i\mathbf{k}(t) \times (\mathbf{k}(t) \times \hat{\mathbf{e}}) - \lambda|\mathbf{k}(t)|(\mathbf{k}(t) \times \hat{\mathbf{e}})}{k(t)^2 \sqrt{1 + \lambda^2} \sqrt{1 - (\mathbf{k}(t) \cdot \mathbf{e})^2/k(t)^2}}. \tag{33}$$

The wavenumber 'k' is defined as $2\pi/l$ (where l is the scale size). A value of $k = 1$ corresponds to the large-scale regime, while $k > 2$ refers to the wavenumber in the small (turbulent) scale regime. The parameter $\lambda = \pm 1$ generates a fully right-($\lambda = +1$) or left-handed ($\lambda = -1$) helical field, described by $\nabla \times \mathbf{f}_k \to i\mathbf{k} \times \mathbf{f}_k \to \pm k\mathbf{f}_k$. The choice of $\lambda = +1$ represents right-handed polarization, corresponding to the southern hemisphere, while $\lambda = -1$ represents left-handed polarization for the northern hemisphere. Here, $\hat{\mathbf{e}}$ denotes an arbitrary unit vector. We applied fully helical kinetic energy ($\lambda = \pm 1$) at $\langle k \rangle_{\mathrm{ave}} \equiv k_f \sim 5$. And, we used $f_0 = 0.07$ and $\nu = \eta = 0.006$. Note that Reynolds' rule is not applied to this energy source: $\langle f \rangle \neq 0$. Notably, an initial seed magnetic field of $B_0 \sim 10^{-4}$ was introduced into the system. However, the influence of this seed field diminishes rapidly due to the presence of the forcing function and the lack of memory in the turbulent flow.

B. Numerical Results

Figure 3 shows the energy, helicity, and averaged velocity and magnetic field in a kinetically driven plasma system. The left panel presents the southern hemisphere, which generates positive (right-handed) kinetic helicity, while the right panel shows the northern hemisphere, which generates negative (left-handed) kinetic helicity. Figures 3(a) and 3(b) depict the magnetic energy spectrum E_M (red solid line) and kinetic energy spectrum E_V (black dashed line) in Fourier space at times $t = 0.2, 100, 200$, and 1440, showing the evolution of the energy spectra. As observed, the energy spectra for the southern and northern hemispheres match precisely. Both panels illustrate that the kinetic energy E_V at the forcing scale $k = 5$ is converted into magnetic energy E_M, which is subsequently inverse cascaded to the large scale $k = 1$. At this scale, E_V is significantly low, indicating an insufficient inverse cascade of kinetic energy. Additionally, each energy spectrum $k > 5$ decreases more steeply than the Kolmogorov scale $k^{-5/3}$, implying that the kinetic energy E_V from the forcing scale does not fully cascade down to smaller plasma eddy regions, a limitation arising from the low magnetic Reynolds number $Re_M = 261$.

In Figures 3(c) and 3(d), the kinetic helicity $H_V (= \langle \mathbf{u} \cdot \nabla \times \mathbf{u} \rangle)$ and kinetic energy $2E_V (= \langle u^2 \rangle)$ spectra over time are illustrated, with kinetic helicity represented by the red solid line and kinetic energy by the black dashed line. While the Southern and Northern Hemispheres exhibit similar trends, there is a distinct difference in the sign of kinetic helicity: in Figure 3(c), which pertains to the Northern Hemisphere, the helicity value is negative. Therefore, its absolute value is displayed for consistency. In contrast, Figure 3(d) for the Southern Hemisphere shows positive helicity values, making the absolute value indicator unnecessary. Furthermore, in both hemispheres, for wave numbers $k > 2$, kinetic helicity surpasses kinetic energy. However, as $k \to 1$, the kinetic energy value rises, indicating a more effective forward cascade of kinetic helicity in these regions. This reflects the differences in how helicity and energy cascade within the system, with kinetic helicity showing a more pronounced forward cascade effect.

Figures 3(e) and 3(f) illustrate the average velocity and magnetic field in both the Northern and Southern Hemispheres. Using the data from Figures 3(a) and 2(b), we calculate $U_{\mathrm{rms}} = \sqrt{\sum_k 2E_V}$ and $B_{\mathrm{rms}} = \sqrt{\sum_k 2E_M}$. The resulting values are $U_{\mathrm{rms}} \approx 0.14$ and $B_{\mathrm{rms}} \approx 0.25$, which correspond to $Re \approx 146$ and $Re_M \approx 241$. Although the system is characterized by $Pr_M = 1$ with $\eta = \nu = 0.006$, the observed difference between Re and Re_M is expected, as the momentum equation and the magnetic induction equation are coupled. Furthermore, the fact that $Re_M > Re$ indicates that a greater portion of energy is transferred to smaller-scale magnetic eddy regions, which aligns with typical outcomes of the dynamo process. Of course, for real stars or the Sun, the Reynolds number is extremely high, and the magnetic Prandtl number is also much smaller than 1. Here, we have limited our model to a simpler case to investigate the effect of helicity with opposite polarities in the Northern and Southern Hemispheres on the overall formation of the solar magnetic field.

Figures 4(a), 4(b) shows the magnetic helicity $H_M (= \langle \mathbf{A} \cdot \mathbf{B} \rangle)$ and magnetic energy $2E_M (= \langle B^2 \rangle)$ in the Northern and Southern Hemispheres. Absolute values are used here to facilitate comparison with energy, though in reality, these values depend on the wavenumber k. In the Northern Hemisphere, kinetic helicity is negative, while in the Southern Hemisphere, it is positive. Magnetic helicity at the k=1 takes on the opposite sign to kinetic helicity but aligns with it in the remaining region, conserving magnetic helicity. Notably, in the saturation state, the magnetic energy and magnetic helicity at k=1 are equal in magnitude, whereas in other regions, the energy is greater.

Figures 4(c) and 4(d) compare the magnetic helicity and magnetic energy in large-scale regions of the Northern and Southern Hemispheres. The magnetic helicity is presented as an absolute value, as its sign differs in each hemisphere, as discussed above. Additionally, both the difference and summation of $\langle \overline{B}^2 \rangle$ and $\langle \overline{\mathbf{A}} \cdot \overline{\mathbf{B}} \rangle$ are used to determine the values of α and β [see Eqs. (20), (21)].

Figures 5(a) and 5(b) compare the current helicity $\langle \mathbf{J} \cdot \mathbf{B} \rangle (= k^2 H_M)$ with the magnetic energy multiplied by the wave number $k \langle B^2 \rangle$ across the entire Fourier space. In Figure 5(a), which represents the Southern Hemisphere, note that the signs of $\langle \mathbf{J} \cdot \mathbf{B} \rangle (= k^2 H_M)$ and $k \langle B^2 \rangle$ are opposite in the large-scale region where $k = 1$, while they are the same on other scales. This results from the positive kinetic helicity generated by buoyancy and the leftward-deflecting Coriolis force in the Southern Hemisphere. The field structure in Figure 2(b) corresponds to the southern hemisphere. Conversely, Figure 5(b) shows the opposite behavior in the Northern Hemisphere.

Figures 5(c) and 5(d) display the kinetic helicity ratio $f_{hk} (= \langle \mathbf{U} \cdot \omega \rangle / k \langle U^2 \rangle)$ (black) and the magnetic helicity ratio $f_{hm} (= k \langle \mathbf{A} \cdot \mathbf{B} \rangle / \langle B^2 \rangle)$ (red) for $k = 1, 5, 8$. In the Southern Hemisphere, f_{hk} at the forcing scale, where $k = 5$, is $+1$, and f_{hk} in other regions maintains somewhat positive values. On the other hand, f_{hm} converges to -1 when $k = 1$, with values in other small-scale regions converging to positive values. The opposite phenomenon occurs in the Northern Hemisphere, as shown in the right panel.

Figures 6(a) and 6(b) compare the $\alpha_{\text{EM−HM}}$ coefficients obtained using large-scale magnetic data [Eq. (20)] with the α_{MFT} coefficients approximated using small-scale kinetic and magnetic data [Eq. (7)]. The left panel shows the Southern Hemisphere, while the right panel shows the Northern Hemisphere. As Figure 6(a) indicates, when the plasma system is driven with positive kinetic helicity, the α effect decreases from positive to negative and then converges to 0. Conversely, when the system is driven with negative kinetic helicity, as shown in Figure 6(b), the α effect maintains a positive value before converging to 0. The MFT method requires integrating residual helicity over time, given by $\frac{1}{3} \int^{\tau} (\langle \mathbf{j} \cdot \mathbf{b} \rangle - \langle \mathbf{u} \cdot \omega \rangle)\, dt$, but since the exact time range is unknown, only the residual helicity and the coefficient $\frac{1}{3}$ are considered here. Also, we calculated α_{MFT} values across cases of $k = 2 - 4$, $k = 2 - 6$, and $k = 2 - k_{\max}$. In both hemispheres, $\alpha \sim 0$ is obtained for $k = 2 - 4$, and there is no difference in α between $k = 2 - 6$ and $k = 2 - k_{\max}$, indicating that the forcing scale $k = 5$ primarily determines α. The α effect obtained through MFT was initially considered to play a significant role in magnetic field amplification. However, this conclusion is incomplete, as α_{MFT} incorporates only the leading-order terms and does not account for the effects of higher-order terms. The discrepancy between $\alpha_{\text{EM−HM}}$ and α_{MFT} suggests a role for the neglected higher-order terms quenching the α effect, thereby playing a limited role in magnetic field amplification. Additionally, this is consistent with the fact that the phase difference between the magnetic fields B_{pol} and B_{tor} in the actual Sun is $\pi/2$. According to the coupled harmonic oscillator model in classical mechanics, when the coupling coefficient α is large, the possible modes are the 0 mode and the π mode, and such a weak coupling mode cannot appear [33].

Figures 6(c) and 6(d) illustrate the magnetic diffusion, or β effect. Here, we compare $\beta_{\text{EM−HM}}$, obtained from large-scale magnetic data [Eq. (21)]; β_{MFT}, derived from plasma turbulent kinetic energy [Eq. (8)]; and $\beta_{\text{VV−HV}}$, calculated using both plasma turbulent kinetic energy and kinetic helicity [Eq. (32)]. The coefficient $\beta_{\text{EM−HM}}$ maintains a negative value before converging to zero. Since the β effect is represented as $\beta \nabla^2 \rightarrow -\beta k^2$ in conjunction with the Laplacian operator, this behavior contributes to the diffusion of the magnetic field toward large scales and amplifies magnetic field density. Similar effects are observed for $\beta_{\text{EM−HM}}$ in both the Northern and Southern Hemispheres, and $\beta_{\text{EM−HM}}$ is not influenced by the polarity of helicity (see Figure 2(b)). Meanwhile, β_{MFT}, specifically β_{vv}, remains positive, yielding a negative effect in conjunction with the Laplacian, which ultimately serves to decrease magnetic field energy. However, this result only accounts for the leading term, without considering the helical component of plasma kinetic energy. By contrast, $\beta_{\text{VV−HV}}$, which incorporates both kinetic energy and kinetic helicity, aligns closely with $\beta_{\text{EM−HM}}$, suggesting that the kinetic helicity effect of the plasma is crucial to the actual magnetic diffusion effect. On the other hand, $\beta_{\text{EM−HM}}$ is negligibly small within the $k = 2$–4 range. The lack of significant difference between $\beta_{\text{EM−HM}}$ across the $k = 2$–6 and $k = 2$–$k_{\max}$ regions indicates that the external forcing scale at $k = 5$ substantially impacts the system.

In terms of observations, $\beta_{EM−HM}$, which requires information on large-scale magnetic fields, is more useful than $\beta_{VV−HV}$, which relies on data from turbulent regions. However, since $\beta_{VV−HV}$ includes insights into plasma activity within the celestial plasma systems, further research into $\beta_{VV−HV}$ is needed, especially as it reproduces the profile of $\beta_{EM−HM}$. The alignment of $\beta_{EM−HM}$ and $\beta_{VV−HV}$ in the $10 < t < 250$ range—before nonlinear magnetic effects intensify and after initial conditions disappear—suggests the critical, independent role of kinetic helicity in magnetic field amplification through diffusion. Moreover, the discrepancy observed in the region where the magnetic field undergoes significant amplification ($t >\sim 250$) indicates that $\beta_{VV−HV}$ should incorporate effects related to the magnetic field itself.

Figures 7(a) and 7(b) present a comparison between α and β parameters with EMF from DNS. What we require is $\langle \mathbf{u} \times \mathbf{b} \rangle$ in the turbulent region, but since the range is uncertain, we used $\partial \overline{\mathbf{B}}/\partial t - \eta \nabla^2 \overline{\mathbf{B}}$, which corresponds to $\nabla \times \langle \mathbf{u} \times \mathbf{b} \rangle$. In contrast, $\nabla \times (\alpha \overline{\mathbf{B}} - \beta \nabla \times \overline{\mathbf{B}})$ can be directly calculated for each case. We compare $(\alpha_{EM−HM}, \beta_{EM−HM})$ with $(\alpha_{EM−HM}, \beta_{VV−VW})$, finding that the DNS result aligns closely with $(\alpha_{EM−HM}, \beta_{EM−HM})$. This confirms the accuracy of $\alpha_{EM−HM}$ and $\beta_{EM−HM}$. Conversely, $(\alpha_{EM−HM}, \beta_{VV−VW})$ is consistent with the others only within the $t < 300$ region. Given that $\alpha_{EM−HM}$ is not particularly large, this suggests that $\beta_{vv−vw}$ remains valid while the magnetic field effect is moderate. However, as the magnetic field effect intensifies, turbulent kinetic energy and kinetic helicity alone become insufficient. Figures 7(c) and 7(d) illustrate the ratio of $\beta_{vv−vw}$ to $\beta_{EM−HM}$. In the range $10 < t < 250 - 300$, the ratio is close to 1, but for $t > 250 - 300$, $\beta_{vv−vw}$ exhibits significantly larger oscillations.

Figures 8(a) and 8(b) display the large-scale kinetic energy ($10 \times \overline{E}_V$, shown as the black dot-dashed line) and magnetic energy ($10 \times \overline{E}_M$, shown as the red solid line). Around $t \sim 200 - 400$, $\overline{E}_M$ shows a noticeable increase and eventually reaches a saturation point, while $\overline{E}_V$ remains low throughout. Both $\overline{E}_V$ and $\overline{E}_M$ are scaled by a factor of 10 to enhance their visibility. The plots also include the temporal profiles of the α (dotted line) and β (dashed line) coefficients, derived from large-scale magnetic energy and helicity. These results clearly demonstrate the relationships among $\overline{E}_M$, $\overline{E}_V$, α, and β. A closer inspection of the Southern and Northern Hemispheres reveals that the sign of α is opposite in each hemisphere, and there is a slight difference in the β profile. The sign reversal in α is due to the differing polarity of kinetic helicity, resulting from the Coriolis force direction, while the minor variations in the β profile appear to arise from random selection and initial conditions. In plasma composed of many

charged particles, magnetic field amplification can be understood through the electromagnetic processes described by Ampère's law and the magnetic diffusion effect, which approximates the plasma as a fluid. From the equation $\partial \overline{B} / \partial t = \alpha \overline{J} + (\beta + \eta) \nabla^2 \overline{B}$, the small value of α and the negative value of β suggest a mechanism where electromagnetic properties influence the magnetic field polarity, while diffusion of magnetic eddies facilitates amplification.

Figures 8(c) and 8(d) display the large-scale magnetic fields reproduced using three different combinations of coefficients: $(\alpha_{EM-HM}, \beta_{EM-HM})$, $(\alpha_{EM-HM}, \beta_{VV-HV})$, and $(\alpha_{MFT}, \beta_{MFT})$. These results are compared against the direct numerical simulation (DNS) results to assess the accuracy and efficacy of each coefficient pairing. We used the equation below to calculate the magnetic field.

```
B[0] =  sqrt(2.0*spec_mag(1, 0))  % k=1 for large scale

for j=0L,  t_last do begin
  B[j+1] = B[j] + (sign*alpha[j]-beta[j]-eta)*B[j]*(time[j+1]-time[j])     % helical magnetic field
endfor
```

Here, the time interval $\Delta t \sim 0.2$ and the correlation length $l = 2\pi/3$ are used. The sign in front of α is positive ('+') for the Northern Hemisphere (left-handed kinetic helicity) and negative ('−') for the Southern Hemisphere (right-handed kinetic helicity). Among the configurations, $(\alpha_{EM-HM}$ & $\beta_{EM-HM})$ yields the most accurate results, while the classical MFT method shows the lowest accuracy. This trend is consistent with the results observed in Figures 5 and 6. Meanwhile, $(\alpha_{EM-HM}$ & $\beta_{VV-HV})$ provides relatively accurate results in the kinematic regime before the magnetic field intensifies significantly. However, as the magnetic field grows, β_{VV-HV} deviates by becoming larger than the actual value, likely due to limitations in the statistical model which does not fully account for the magnetic field effects. Furthermore, while a minor difference in magnetic field behavior is noted between the northern and southern hemispheres, it remains uncertain whether such subtle differences in solar magnetic field formation could indeed result in non-periodic characteristics. The Sun itself is a nearly axisymmetric sphere, but its slightly tilted rotation axis (7.25°) and the gravitational influence of surrounding planets are likely to affect the α and β effects.

The reproduced Figs.9(a)-9(d) confirm the dependence of α and β on turbulent kinetic helicity [1]. Since these figures directly illustrate the influence of kinetic helicity on the β effect, we reproduce them here for further discussion. The system was driven with positively helical kinetic energy at $k = 5$ until $t = 210$. Then, while keeping the total energy constant, we removed the helical component by changing λ from 1 to 0 (see Eq. (33)). We then examined how the large-scale magnetic field, α, and β evolved.

Fig. 9(a) shows a sudden drop in large-scale magnetic energy and helicity due to the cessation of energy input and the dissipative effects of $\beta + \eta$.

Fig. 9(b) illustrates the changes in the helicity ratios of kinetic and magnetic eddies at k =1, 5, 8, representing the large scale, forcing scale, and small scale, respectively. For $t < 210$, the system follows the standard helical forcing regime. However, after helicity is removed, the helicity ratio converges to zero in most cases. Nonetheless, at small scales, a nonzero helicity region persists for some time.

Fig. 9(c) presents the evolution of α_{EM-HM} (dot-dashed line) and α_{MFT} (solid lines). α_{EM-HM} approaches zero much earlier than changes in the helicity ratio, indicating that it is less affected by the removal of helicity. In contrast, α_{MFT} for $k = 2 - 6$ and $k = 2 - k_{\max}$, initially exhibiting large negative values, rapidly converges to zero. Notably, the behavior of α_{MFT} depends on the forcing scale $k = 5$, while α_{MFT} for $k = 2 - 4$ does not contribute significantly to the system.

Fig. 9(d) directly demonstrates the dependence of β on kinetic helicity. β_{MFT} (dotted line), which depends on $\langle V^2 \rangle$, remains largely unaffected by helicity variations. In contrast, β_{EM-HM} and β_{vv-vw} are strongly influenced by H_V, retaining negative values until $t = 210$. During $t \sim 10 - 210$, their profiles remain consistent despite being derived from different datasets and theoretical frameworks. Specifically, β_{EM-HM} is computed from large-scale magnetic data using differentiation, while β_{vv-vw} is obtained from turbulent kinetic data through integration. As the system stabilizes under helical forcing, their profiles become increasingly aligned. When helicity $\langle \mathbf{v} \cdot \omega \rangle$ is removed, both values abruptly increase, become positive, and converge to β_{MFT}. This consistency in the absence of helicity provides strong evidence for the dependence of the β effect on kinetic helicity. The evolutions of various α and β values are consistent with Eqs. (20), (21), and (32). In particular, when $H_V \rightarrow 0$, $\beta_{\text{EM–HM}} \sim \beta_{\text{vv–vw}} \sim \beta_{\text{MFT}}$.

Recently, Igor et al.[34] proposed a turbulent magnetic diffusion coefficient η_t using path integrals. By employing a projection operator, Taylor expansion, second-order moments of velocity, Fourier transforms, and tensor identities, they derived η_t, which can take negative values, and compared it with simulation results. They found a qualitative result that the magnetic diffusivity decreases when kinetic helicity is present. However, they have not yet reproduced the magnetic field in DNS, and their results only show the diffusivity based on the helicity ratio at saturation, rather than the time-dependent variation. As intuitively shown

in Figure 2, when kinetic helicity is present, u_p exists, and this velocity component combines with b_{ind} and B_0 to generate new current densities and magnetic fields. This is expressed as a negative β, which, when combined with the Laplacian $\nabla^2 \to -k^2$, leads to an increase in magnetic field strength. This is confirmed in Fig. 9(d).

V. SUMMARY

We calculated the α and β effects generated by kinetic helicity, which has opposite signs in the southern and northern hemispheres of a rotating astrophysical plasma system like the Sun. And, we reproduced the large-scale magnetic field and compared it with DNS result. The rotating fluid inherently exhibits buoyancy and Coriolis forces, with the Coriolis force acting in opposite directions in the northern and southern hemispheres. As a result, the α coefficients in both hemispheres have opposite signs, forming current densities that are either parallel or antiparallel to the magnetic flux. These, in turn, create poloidal magnetic fields that flow in opposite directions above and below the magnetic flux, where the B_{pol} positioned below the magnetic flux forms a new magnetic flux in the opposite direction due to differential rotation. As the magnetic density increases, particle density decreases, causing the magnetic flux to become lighter and interact with the existing magnetic flux at the surface. Interestingly, the direction of the current density remains constant relative to the magnetic flux that changes direction periodically. By determining the α and β effects based on the polarity of kinetic helicity, we reproduced the large-scale magnetic field and compared it with DNS results.

The analysis revealed that the sign of α profile depends on the hemisphere, while the β profile remains the same. The α effect is relatively small, and the β effect is significant, indicating that fluid diffusion effects play a larger role than electromagnetic properties in a plasma composed of many charged particles. However, despite its smaller magnitude, the α effect cannot be ignored as it plays a crucial role in determining the overall polarity of helical magnetic field structures. Negative β indicates that the energy in the turbulent region is diffusing into the large-scale magnetic field. In the case of a non-helical field, β takes on a positive value diffusing energy. If helical structures of u_p are present, the β effect adopts a negative value that amplifies the magnetic field (Fig. 2). The α and β coefficients derived from the large-scale magnetic data reproduce the magnetic fields obtained through DNS very accurately. However, since this is the result of all combined physical effects, more detailed analysis is necessary. We used turbulent kinetic energy & kinetic helicity to derive the β coefficient and utilized DNS kinetic data to reproduce the large-scale magnetic field for comparison with other results. In the kinematic regime where the magnetic field strength is not strong, all results align well; however, in regions where the magnetic field effect becomes non-linear and strong, the reproduced magnetic field appears larger than reality due to insufficient quenching of the β effect. This fundamentally arises from the inability to incorporate the magnetic field effect in Eqs. (23)-(26). Since velocity u is a function of the magnetic field in a plasma, it is evident that the statistical identity for the second moment of u should include the magnetic field effect. This will be addressed through a complete solution of the MHD equations, which is beyond the scope of this article. Nonetheless, it is clear that incorporating the magnetic field effect into the statistical identity will significantly enhance the accuracy of the β coefficient. The methods used to calculate α and β, along with the comparison of their results, are summarized in the table below.

TABLE I. Comparison of Methods for Calculating α and β and Their Impact on $\overline{B}$

Method	Data Used	Calculation Method	Accuracy of $\overline{B}$
α_{MFT} & β_{MFT}	Turbulent kinetic and magnetic data	Integral	Inaccurate
α_{EM-HM} & β_{EM-HM}	Large-scale magnetic data	Differentiation	Accurate
α_{EM-HM} & β_{vv-vw}	Turbulent kinetic data	Integral (diff. for α)	Accurate for weak $\overline{B}$

In this paper, we considered the case of a rotating plasma sphere with $Pr_M = 1$ and low Reynolds numbers. However, in reality, Reynolds numbers are very high, and Pr_M is much less than 1, which necessitates further general studies on this topic that we plan to address in future research.

Data Availability
All data are incorporated into the article and its online supplementary material.

ACKNOWLEDGEMENTS

---

[1] K. Park, Phys. Rev. D **111**, 023021 (2025).

[2] E. N. Parker, Astrophys. J. **122**, 293 (1955).

[3] H. W. Babcock, Astrophys. J. **133**, 572 (1961).

[4] R. B. Leighton, Astrophys. J. **156**, 1 (1969).

[5] P. Charbonneau, Advances in Space Research **39**, 1661 (2007).

[6] R. H. Kraichnan, Journal of Fluid Mechanics **75**, 657 (1976).

[7] A. Brandenburg and D. Sokoloff, Geophysical and Astrophysical Fluid Dynamics **96**, 319 (2002), arXiv:astro-ph/0111568 [astro-ph].

[8] A. B. Bendre, J. Schober, P. Dhang, and K. Subramanian, mnras **530**, 3964 (2024), arXiv:2308.00059 [astro-ph.GA].

[9] A. Lanotte, A. Noullez, M. Vergassola, and A. Wirth, Geophysical and Astrophysical Fluid Dynamics **91**, 131 (1999).

[10] A. Giesecke, F. Stefani, and G. Gerbeth, New Journal of Physics **16**, 073034 (2014), arXiv:1405.5788 [physics.flu-dyn].

[11] S. Cabanes, N. Schaeffer, and H.-C. Nataf, Phys. Rev. Lett. **113**, 184501 (2014), arXiv:1411.6366 [physics.flu-dyn].

[12] M. Schrinner, K.-H. Rädler, D. Schmitt, M. Rheinhardt, and U. Christensen, Astronomische Nachrichten **326**, 245 (2005).

[13] K. Park, Phys. Rev. D **96**, 083505 (2017).

[14] K. Park, Astrophys. J. **872**, 132 (2019), arXiv:1808.01226.

[15] K. Park, M. K. Cheoun, and C.-B. Kim, Astrophys. J. **944**, 2 (2023).

[16] J. M. Stone, T. A. Gardiner, P. Teuben, J. F. Hawley, and J. B. Simon, apjs **178**, 137 (2008), arXiv:0804.0402 [astro-ph].

[17] M. Steenbeck and F. Krause, Zeitschrift Naturforschung Teil A **21**, 1285 (1966).

[18] H. K. Moffatt, *Magnetic field generation in electrically conducting fluids*, edited by Moffatt, H. K. (Cambridge, England, Cambridge University Press, 1978. 353 p., 1978).

[19] F. Krause and K. Rädler, *Mean-field magnetohydrodynamics and dynamo theory*, edited by Goodman, L. J. & Love, R. N. (Oxford, Pergamon Press, Ltd., 1980. 271 p., 1980).

[20] A. Yoshizawa, *Hydrodynamic and Magnetohydrodynamic Turbulent Flows* (Springer, 2011).

[21] R. H. Kraichnan and S. Nagarajan, Physics of Fluids **10**, 859 (1967).

[22] A. Pouquet, U. Frisch, and J. Leorat, Journal of Fluid Mechanics **77**, 321 (1976).

[23] P. Charbonneau, ARA&A **52**, 251 (2014).

[24] G. B. Rybicki and A. P. Lightman, *Radiative Processes in Astrophysics* (1986).

[25] K. Park and E. G. Blackman, MNRAS **419**, 913 (2012), arXiv:1108.6079 [astro-ph.IM].

[26] U. Frisch, A. Pouquet, J. Leorat, and A. Mazure, Journal of Fluid Mechanics **68**, 769 (1975).

[27] E. Devlen, A. Brandenburg, and D. Mitra, MNRAS **432**, 1651 (2013), arXiv:1212.2626 [astro-ph.SR].

[28] A. Andrievsky, A. Brandenburg, A. Noullez, and V. Zheligovsky, apj **811**, 135 (2015), arXiv:1501.04465 [physics.flu-dyn].

[29] P. J. Käpylä, M. J. Korpi, and A. Brandenburg, aap **500**, 633 (2009), arXiv:0812.1792 [astro-ph].

[30] M. J. Käpylä, J. Á. Vizoso, M. Rheinhardt, A. Brandenburg, and N. K. Singh, Astrophys. J. **905**, 179 (2020), arXiv:2006.05661 [physics.flu-dyn].

[31] K. Park, Astrophys. J. **898**, 112 (2020), arXiv:1911.01039 [astro-ph.SR].

[32] M. Lesieur, *Turbulence in Fluids, by Marcel Lesieur. Series: Fluid Mechanics and Its Applications. Berlin: Springer, 2008.* (2008).

[33] H. Goldstein, C. Poole, and J. Safko, *Classical mechanics* (2002).

[34] I. Rogachevskii, N. Kleeorin, and A. Brandenburg, arXiv e-prints , arXiv:2501.13807 (2025), arXiv:2501.13807 [physics.flu-dyn].